Research Paper

# Metasomatism-induced wehrlite formation in the upper mantle beneath the Nógrád-Gömör Volcanic Field (Northern Pannonian Basin): Evidence from xenoliths

Levente Patkó [a,b], Nóra Liptai [a,c], László Előd Aradi [a], Rita Klébesz [d], Eszter Sendula [e], Robert J. Bodnar [e], István János Kovács [f], Károly Hidas [g], Bernardo Cesare [h], Attila Novák [d], Balázs Trásy [i], Csaba Szabó [a,*]

[a] Lithosphere Fluid Research Lab, Institute of Geography and Earth Sciences, Eötvös Loránd University, Budapest, Hungary
[b] Isotope Climatology and Environmental Research Centre, Institute for Nuclear Research, Hungarian Academy of Sciences, Debrecen, Hungary
[c] CCFS-GEMOC, Department of Earth and Planetary Sciences, Macquarie University, Sydney, Australia
[d] Geodetic and Geophysical Institute, Research Centre for Astronomy and Earth Sciences, Hungarian Academy of Sciences, Sopron, Hungary
[e] Fluids Research Laboratory, Department of Geosciences, Virginia Tech, Blacksburg, VA, United States
[f] MTA CSFK Lendület Pannon LitH$_2$Oscope Research Group, Geodetic and Geophysical Institute, Research Centre for Astronomy and Earth Sciences, Hungarian Academy of Sciences, Sopron, Hungary
[g] Instituto Andaluz de Ciencias de La Tierra, CSIC & UGR, Armilla, Granada, Spain
[h] Department of Geosciences, University of Padua, Padua, Italy
[i] Department of Geology, Eötvös Loránd University, Budapest, Hungary

## ARTICLE INFO

## ABSTRACT

Clinopyroxene-enriched upper mantle xenoliths classified as wehrlites are common (~20% of all xenoliths) in the central part of the Nógrád-Gömör Volcanic Field (NGVF), situated in the northern margin of the Pannonian Basin in northern Hungary and southern Slovakia. In this study, we thoroughly investigated 12 wehrlite xenoliths, two from each wehrlite-bearing occurrence, to determine the conditions of their formation. Specific textural features, including clinopyroxene-rich patches in an olivine-rich lithology, orthopyroxene remnants in the cores of newly-formed clinopyroxenes and vermicular spinel forms all suggest that wehrlites were formed as a result of intensive interaction between a metasomatic agent and the peridotite wall rock. Based on the major and trace element geochemistry of the rock-forming minerals, significant enrichment in basaltic (Fe, Mn, Ti) and high field strength elements (Nb, Ta, Hf, Zr) was observed, compared to compositions of common lherzolite xenoliths. The presence of orthopyroxene remnants and geochemical trends in rock-forming minerals suggest that the metasomatic process ceased before complete wehrlitization was achieved. The composition of the metasomatic agent is interpreted to be a mafic silicate melt, which was further confirmed by numerical modelling of trace elements using the plate model. The model results also show that the melt/rock ratio played a key role in the degree of petrographic and geochemical transformation. The lack of equilibrium and the conclusions drawn by using variable lherzolitic precursors in the model both suggest that wehrlitization was the last event that occurred shortly before xenolith entrainment in the host mafic melt. We suggest that the wehrlitization and the Plio–Pleistocene basaltic volcanism are related to the same magmatic event.

## 1. Introduction

A significant number of dunite, harzburgite and pyroxene-rich xenoliths occur in combination with the dominant lherzolites hosted in alkali basaltic, lamprophyric and kimberlitic magmas worldwide, indicating different stages of geochemical depletion or enrichment (e.g., Downes, 2001 and references therein). Xenoliths with high orthopyroxene content are common among the pyroxene-rich rocks and have been

---

the focus of most xenolith studies (Kelemen et al., 1992, 1998; Smith et al., 1999; Bali et al., 2007; Woo et al., 2014). Less attention has been paid to the petrogenesis of clinopyroxene-enriched upper mantle xenoliths, i.e. wehrlites. Wehrlites are unlikely to represent partial melting residues of peridotite (e.g., Kelemen, 1990).

Two processes are commonly invoked to explain the formation of wehrlites: either they represent high pressure cumulates that crystallized from melts trapped near the crust-mantle transitional zone, forming lenses or dikes (Frey and Prinz, 1978; Girardeau and Francheteau, 1993; Rocco et al., 2013) or they may result from metasomatism triggered by fluid/melt-peridotite interaction. The metasomatic agent of wehrlitization can be carbonate melt/fluid, producing magnesian wehrlites (e.g., Hauri et al., 1993; Rudnick et al., 1993; Yaxley et al., 1998; Coltorti et al., 1999; Kogarko et al., 2001; Scott et al., 2014) or silicate melts leading to the formation of Fe-rich wehrlites (e.g., Zinngrebe and Foley, 1995; Peslier et al., 2002; Rivalenti et al., 2004; Shaw et al., 2005, 2018).

The wehrlite suite represented in several xenolith–bearing localities of the Nógrád-Gömör Volcanic Field (Carpathian–Pannonian region, northern Hungary–southern Slovakia) (Fig. 1) provides the opportunity



**Fig. 1. (a)** Simplified geological map of the Carpathian-Pannonian region with the inferred ALCAPA-Tisza-Dacia microplate boundary (after Csontos and Nagymarosy, 1998 and references therein). Xenolith-bearing Neogene alkali basalt occurrences shown are the following: SBVF, Styrian Basin Volcanic Field; LHPVF, Little Hungarian Plain Volcanic Field; BBHVF, Bakony–Balaton Highland Volcanic Field; NGVF, Nógrád-Gömör Volcanic Field; PMVF, Perşani Mountains Volcanic Field. **(b)** Alkali basalt occurrences and wehrlite sampling locations in the Nógrád-Gömör Volcanic Field; quarries or outcrops from NW to SE are Trebeľovce (NTB), Fiľakovské Kováče (NFK), Ratka (NFR), Mačacia (NMC), Magyarbánya (NMM) and Eresztvény (NME).

for a detailed petrographic and geochemical study of the conditions of wehrlitization. A thorough examination of the differences within single xenoliths and between xenoliths has revealed significant small-scale heterogeneities that suggest specific evolution paths. Hence, our study contributes to a better understanding of the nature of the metasomatic process that leads to the formation of wehrlitic mantle domains.

Here, we report detailed petrographic, and major and trace element geochemical data for 12 selected wehrlite xenoliths and are interpreted here to have been formed by mafic melt interaction with peridotite wall rock. To support our interpretations, the composition of the equilibrium melt was estimated through bulk trace element modelling using the plate model of Vernières et al. (1997). The occurrences of wehrlite xenoliths were compared to the results of local deep geophysical surveys (Novák et al., 2014), which suggest that wehrlitization may have affected a large volume (hundreds of km$^3$) of the local upper mantle, as evidenced by an unusually high local conductivity (1–10 Ωm). This indicates that the magmatism beneath intraplate volcanic fields may be more extensive than was previously thought based only on the areal extent and volume of erupted products (cf., Downes et al., 2004). Our results have application beyond the Carpathian–Pannonian region, and have important implications for developing a more refined understanding of wehrlitisation in the vicinity of alkali basaltic volcanic fields worldwide.

## 2. Geological setting

The Pannonian Basin is situated in East–Central Europe surrounded by the Alpine, Carpathian and Dinaric orogenic belts (Fig. 1a). Understanding the complex tectonic evolution of this extensional back-arc basin has been the focus of many studies (e.g., Royden et al., 1982; Horváth, 1993; Csontos, 1995; Fodor et al., 1999; Bada and Horváth, 2001; Horváth et al., 2006; Schmid et al., 2008; Kovács et al., 2012; Balázs et al., 2016). The Pannonian Basin consists of two different tectonic mega-units referred to as ALCAPA in the northwest and Tisza-Dacia in the southeast (Stegena et al., 1975; Balla, 1984; Kázmér and Kovács, 1985; Csontos et al., 1992; Csontos and Vörös, 2004), divided by the Mid-Hungarian Shear zone (Fig. 1a) (Kázmér and Kovács, 1985; Csontos and Nagymarosy, 1998; Fodor et al., 1998). The juxtaposition of the ALCAPA and Tisza-Dacia blocks by extrusion (Kázmér and Kovács, 1985; Ratschbacher et al., 1991; Horváth, 1993) occurred during the latest Oligocene to early Miocene. Their lateral motion was closely related to the northward movement of the Adriatic microplate and slab rollback (Csontos et al., 1995; Fodor et al., 1999), and accompanied by asthenospheric flow (Kovács et al., 2012). During this stage, significant thinning of the lithosphere and subsequent asthenospheric doming took place in the Pannonian Basin (Horváth, 1993). Finally, the collision of ALCAPA and Tisza-Dacia with the stable European platform gradually led to a compressive phase starting in late Miocene (Horváth and Cloetingh, 1996).

During the last 21 Ma, widespread volcanism took place in the Carpathian-Pannonian region (CPR) characterized by silicic, calc-alkaline and alkali volcanic products (Szabó et al., 1992; Harangi, 2001; Kovács and Szabó, 2008; Lexa et al., 2010). In the study area, both garnet-bearing calc-alkaline and alkali volcanic rocks are present (Fig. 1b). The formation of monogenetic alkali basalt volcanic fields consisting of maars, diatremes, tuff cones, cinder/spatter cones and lava flows, such as the Nógrád-Gömör Volcanic Field (NGVF), have been explained by adiabatic decompression melting of the asthenosphere related to upwelling following the main extension period (Embey-Isztin et al., 1993; Seghedi et al., 2004; Harangi et al., 2015). Alternatively, compression beginning in the tectonic inversion stage of the CPR evolution may have squeezed partial melt out from the asthenospheric dome (Kovács et al., 2018). The volcanic activity in the NGVF took place between 6.17 Ma and 1.35 Ma based on K–Ar dating (Balogh et al., 1981). New results of combined U/Pb and (U–Th)/He geochronometry (Hurai et al., 2013) have slightly extended the period of volcanism (7–0.3 Ma).

The NGVF is the northernmost ultramafic xenolith-bearing alkali basalt locality in the CPR (Fig. 1b). In the NGVF, both Type-I
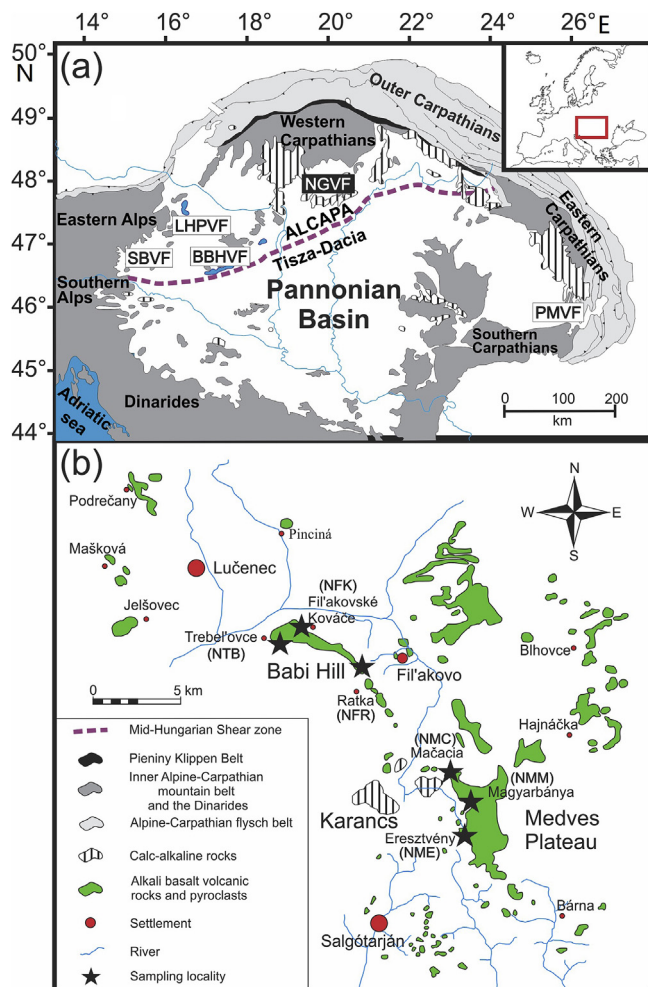
(Embey-Isztin, 1978; Hovorka and Fejdi, 1980; Szabó and Taylor, 1994; Konečný et al., 1995, 1999; Liptai et al., 2017) and Type-II ultramafic rocks (Kovács et al., 2004; Zajacz et al., 2007) have been reported, based on the classification of Frey and Prinz (1978), some with wehrlitic lithology. Liptai et al. (2017) divided the NGVF xenoliths into two groups: Group I, in which the olivine Mg# $\geq$ 89 and Group II, in which the olivine Mg# < 89. Further division was obtained based on rare earth element (REE) depletion ('A' subgroups) or enrichment ('B' subgroups) in clinopyroxenes, respectively. The Group IA and IIA xenoliths are partial melting residues, with subduction-related Nb-poor amphibole formation in the latter. The formation of Group IB and IIB xenoliths are possibly linked to two different metasomatic events, of which the former is characterized by U–Th–Nb–Ta- and light rare earth element (LREE)-enrichment in amphibole and clinopyroxene, whereas the latter resulted in Fe–Mn–Ti-LREE enrichment (Liptai et al., 2017). Xenolith occurrences, based on their different petrographic, geochemical and deformation characteristics can be divided into three main regions: northern (localities Podrečany, Mašková and Jelšovec), central (Babi Hill and Medves Plateau, as well as a separate basalt occurrence, Fil'akovo-Kerčík), and southern (Bárna-Nagykő) (Fig. 1b; Liptai et al., 2017). Wehrlite xenoliths were found only in the central part of the NGVF.

## 3. Sample description

More than 150 xenoliths were collected from six quarries in the two basalt plateaus in the central part of the region, i.e. Medves Plateau (Eresztvény [NME], Magyarbánya [NMM], Mačacia [NMC]) and Babi Hill (Ratka [NFR], Fil'akovské Kováče [NFK], Trebel'ovce [NTB]) (Fig. 1b). Approximately 20% of the xenoltihs were recognized as wehrlites. Based on petrographic features, twelve representative wehrlite xenoliths, two from each location, were selected for detailed petrographic and geochemical study.

The twelve selected alkali basalt lava hosted xenoliths (Table 1) have either angular (NTB1120, NFK1110, NFR1117A, NFR1119B, NME1110, NME1129D) or rounded shapes (NTB1109, NFK1137A, NMC1302B, NMC1343, NMM1114, NMM1129) and range of 3–5 cm in diameter. In some cases, there is evidence of interaction between the host basalt and the xenoliths, including reaction coronas at the margins of xenoliths, consisting of either black clinopyroxenes (NFR1117A, NFR1119B, NME1110, NME1129D) or assemblages of rhönite, augite, magnetite, plagioclase, glass after amphibole breakdown (NTB1120, NFK1110, NMM1114), and minor basalt infiltrations into the xenoliths were observed (NTB1120, NFK1137A, NMC1302B, NMC1343, NME1129D). The studied xenoliths are fresh, with the exception of NMC1302B that shows iddingsite alteration on the rims of olivine.

## 4. Analytical techniques

Petrographic examination of the xenoliths was conducted with a Nikon Eclipse LV100 POL polarizing microscope at the Lithosphere Fluid Research Laboratory (LRG), and with an AMRAY 1830 I/T6 scanning electron microscope at the Department of Petrology and Geochemistry at Eötvös Loránd University (Budapest). Determination of the modal compositions was carried out by applying a point counting method using JMicroVision software (Roduit, 2006), counting at least 500 points per xenolith.

Major element analyses of the rock-forming minerals (olivine, orthopyroxene, clinopyroxene and spinel) were conducted using a CAMECA SX-50 electron microprobe equipped with four wavelength dispersive spectrometers (WDS) and one energy dispersive spectrometer (EDS) in Padua (Italy) at CNR Institute for Geosciences and Earth Resources (IGG). The instrument operated with routine conditions of 20 kV accelerating voltage and 20 nA beam current. Counting times were 10 s at the peak and 5 s at the background for major elements and 20 s at peak and 10 s at the background for minor elements. Standard deviation is $\leq$ 1% for major elements and 3%–5% for minor elements. The oxide weight percentages were obtained from X-ray counts by applying the PAP correction program (Pouchou and Pichoir, 1991).

Trace element analyses of clinopyroxenes were carried out by laser ablation inductively coupled plasma mass spectrometry (LA-ICP-MS) at the Department of Geosciences at Virginia Tech (Blacksburg, VA, USA). The system includes an ArF Excimer laser attached to an Agilent 7500ce quadrupole-based inductively coupled plasma mass spectrometer. The laser acquisition parameters were: 193 nm wavelength, ~7–10 J/cm$^2$ energy density, 5 Hz repetition rate and 32–60 μm spot size. The ablation cell was small in volume (~1.5 cm$^3$) and continuously flushed with He gas at ~1.2 L/min. The auxiliary Ar gas flow was 1.03 L/min, and the reaction cell was used in hydrogen mode. A dwell time of 10 ms per isotope was applied. Following a 60 s gas background analyses with the laser shutter closed, the laser shutter was opened and the sample was ablated for 60 s. The NIST612 synthetic glass (Pearce et al., 1997) was used as the calibration standard and was analyzed twice at the beginning and end of each analytical session to correct for drift. The internal standard was the $^{40}$Ca isotope. Data reduction was carried out by the AMS software (Mutchler et al., 2008).

## 5. Petrography

All xenoliths are identified as wehrlites based on the classification of Streckeisen (1976). They are composed of 72–82 vol.% olivine, with an average of 76 vol.% (Table 1). Clinopyroxene and spinel abundances

**Table 1**
Petrography of the studied NGVF wehrlite xenoliths. The equilibrium temperature calculations are based on the Ca in orthopyroxene thermometer of Nimis and Grütter (2010).

| Sample | Rock name | Texture | Modal composition (%) | | | | | Equilibrium temperature (°C) |
|---|---|---|---|---|---|---|---|---|
| | | | ol | opx | cpx | sp | gl | $T_{Ca-in-opx}$ by NG |
| NTB1109 | wehrlite | fine-grained | 79.0 | 0.5 | 19.0 | 1.0 | 0.5 | – |
| NTB1120 | wehrlite | ol- and cpx-rich patches | 73.0 | 0.5 | 24.0 | 2.0 | 0.5 | – |
| NFK1110 | wehrlite | ol- and cpx-rich patches | 75.0 | 0.5 | 20.5 | 2.0 | 2.0 | – |
| NFK1137A | wehrlite | ol- and cpx-rich patches | 74.5 | – | 23.0 | 2.5 | – | – |
| NFR1117A | wehrlite | ol- and cpx-rich patches | 76.5 | 0.5 | 21.0 | 1.5 | 0.5 | 985 |
| NFR1119B | wehrlite | coarse-grained | 82.5 | 0.5 | 10.0 | 6.5[a] | 0.5 | 1000 |
| NMC1302B | wehrlite | ol- and cpx-rich patches | 74.5 | 0.5 | 22.0 | 1.0 | 1.5 | 1009 |
| NMC1343 | wehrlite | ol- and cpx-rich patches | 77.0 | 0.5 | 20.0 | 1.5 | 1.0 | 1021 |
| NMM1114 | wehrlite | ol- and cpx-rich patches | 72.0 | 0.5 | 23.5 | 3.0 | 1.0 | 1055 |
| NMM1129 | wehrlite | ol- and cpx-rich patches | 80.5 | – | 17.5 | 1.5 | 0.5 | – |
| NME1110 | wehrlite | ol- and cpx-rich patches | 76.0 | 0.5 | 22.0 | 1.5 | – | – |
| NME1129D | wehrlite | ol- and cpx-rich patches | 75.0 | 0.5 | 23.0 | 1.0 | – | – |

Abbreviations: ol–olivine, opx–orthopyroxene, cpx–clinopyroxene, sp–spinell, gl–glass.
[a] Extremely high spinel value is due to a huge interstitial spinel content.

range of 10–24 vol.% and 1–6.5 vol.%, respectively. Orthopyroxene is entirely absent in two xenoliths (NFK1137A, NMM1129) and is observed only as a minor constituent (~0.5 vol.%) in the others. Similarly, up to 2 vol.% of dark glass is observed around small clinopyroxene or spinel grains, except in xenoliths NFK1137A and NME1129D, where it is absent.

The clinopyroxenes and spinels in xenoliths NTB1109 and NFR1119B are disseminated (Supplementary Fig. 1a and b). However, all other wehrlites consist of two, modally and texturally different, irregularly shaped areas represented by olivine- and clinopyroxene-rich assemblages (Fig. 2a) with dimensions of 0.1–1.0 cm.

Olivines in the olivine-rich patches are subhedral, coarse-grained (0.5–1.8 mm) and enclose tiny (50–150 μm) rounded spinels and sometimes orthopyroxene inclusions (Fig. 2b). Rarely, the orthopyroxene

inclusions hosted by olivines are partially surrounded by clinopyroxene (Fig. 2c). The less common interstitial clinopyroxenes and spinels are also subhedral and small (0.2–0.7 mm). Some clinopyroxenes host 70–200 μm orthopyroxene inclusions. The grain boundaries are linear and often meet in 120° triple junctions. Stress joint undulating extinction is sometimes recognized.

Clinopyroxene-rich patches exhibit a poikilitic texture with a 'finger-like' microfabric, whereby fine grained (0.1–0.4 mm), rounded or elongated olivine crystals are enclosed by coarse grained (0.3–0.7 mm), oriented and elongated clinopyroxene oikocrysts with an aspect ratio of 4:1 to 8:1 (Fig. 2d). The entire clinopyroxene-rich patch shows the same extinction. Clinopyroxenes with tabular habit and larger size (5–10 mm) also occur in clinopyroxene-rich patches. Spinel occurs either as
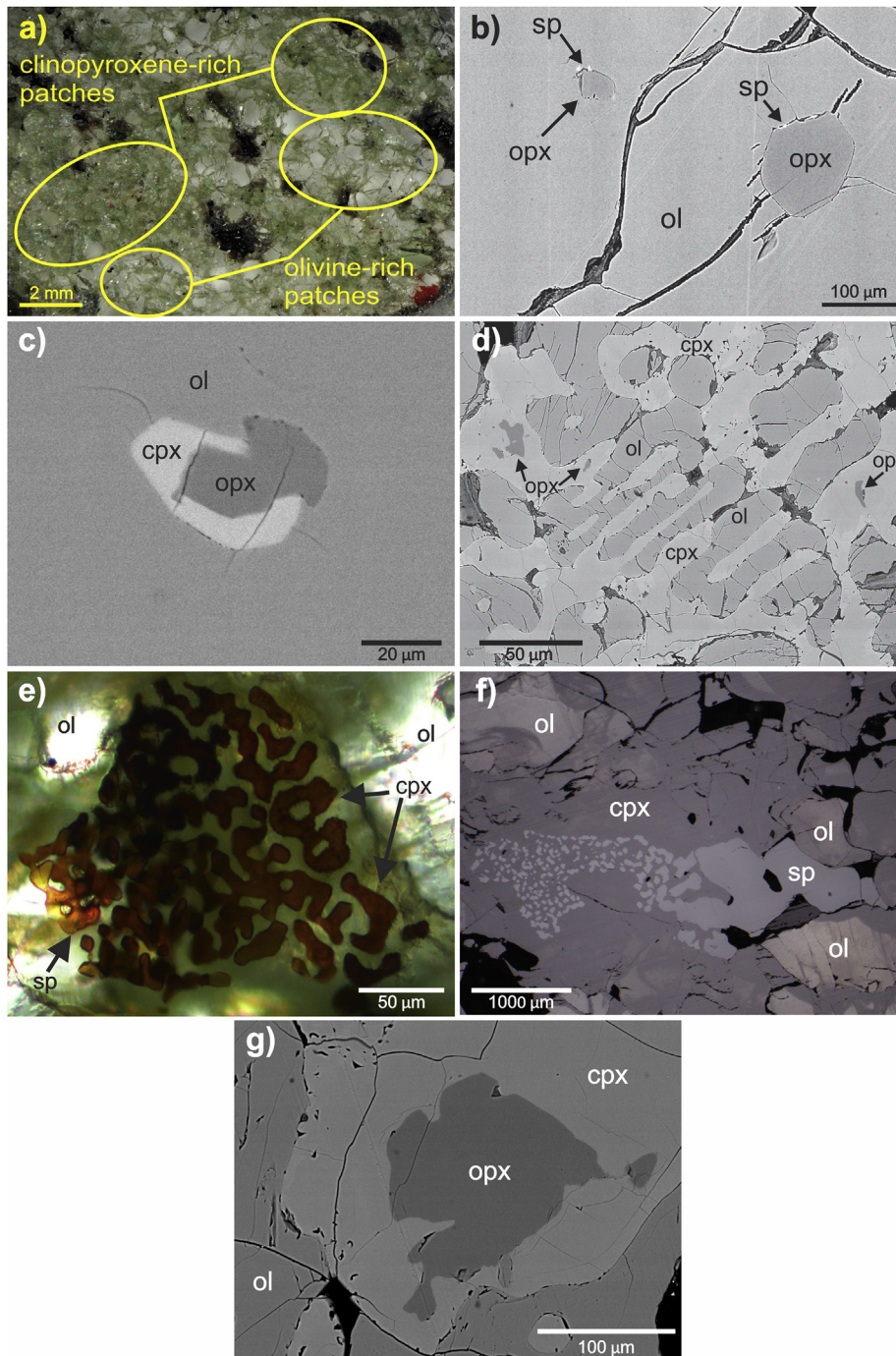


**Fig. 2.** Photomicrographs of wehrlite xenoliths from the Nógrád-Gömör Volcanic Field showing different textural characteristics. **(a)** Typical wehrlitic texture composed of olivine- and clinopyroxene-rich assemblages (stereomicroscopic image) (NMM1129). **(b)** Orthopyroxene inclusions hosted by olivines (back-scattered SEM image) (NFR1119B). Also note spinels at the boundary between the orthopyroxene and the olivine. **(c)** Orthopyroxene inclusion enclosed in olivine with newly formed clinopyroxene at the orthopyroxene-olivine interface (back-scattered SEM image) (NMC1343). **(d)** 'Finger-like' microfabric with elongated olivines and clinopyroxenes. Note that the clinopyroxenes contain tiny orthopyroxene inclusions (back-scattered SEM image) (NFR1117A). **(e)** Vermicular spinels hosted by clinopyroxene (stereomicroscopic image) (NFK1137A). **(f)** Partly vermicular and partly interstitial spinel. Note that the vermicular forms are hosted by clinopyroxenes, while the interstitial segment is adjacent to olivine (reflected light image) (NFK1137A). **(g)** Orthopyroxene inclusion in newly formed clinopyroxene, showing clinopyroxene replacement texture (back-scattered SEM image) (NTB1120).

interstitial spherical grains (0.2–0.9 mm), inclusions in olivine or clinopyroxene (50–150 μm), or as vermicular-shaped grains hosted by clinopyroxenes (Fig. 2e). The vermicular-shaped spinels consist of numerous irregular and tiny (20–40 μm) crystals, and clusters have diameters of 0.1–0.8 mm, similar in size to interstitial spinels and with a 70–30 clinopyroxene/spinel ratio. Although some wehrlites (NTB1109, NTB1120, NFK1137A, NMM1129, NME1129D) contain both interstitial and vermicular spinels, only xenolith NFK1137A contains partly interstitial and partly vermicular single grains displaying a gradual transition between the two forms (Fig. 2f). In such grains, the vermicular spinel portion is always clinopyroxene-hosted, whereas the interstitial portion is adjacent to olivines. In a few patches, 200–400 μm angular or rounded orthopyroxene remnants occur in the cores of clinopyroxene crystals (Fig. 2g). In xenolith NMC1302B, orthopyroxene also occurs in olivine from a clinopyroxene-rich patch. Two wehrlites that do not contain olivine- and clinopyroxene-rich patches have fine-grained (NTB1109) and coarse-grained textures (NFR1119B), with an average grain size of 0.2–0.3 mm and 0.5–0.7 mm, respectively (Supplementary Fig. 1a and b). Mineral constituents in xenolith NTB1109 are mostly rounded, however in wehrlite NFR1119B they are tabular in shape. In wehrlites, a large number of silicate and sulfide melt, and fluid inclusions are present in olivines and clinopyroxenes (Patkó et al., 2018). Details concerning compositions, distribution and significance of these inclusions is the subject of a separate study and will not be discussed here.

## 6. Major element composition of minerals

Significant variations in olivine compositions are observed among the different wehrlite xenoliths (Table 2; Supplementary Table 1). However, olivines within a single xenolith show almost homogeneous chemistry (Fig. 3a) with the exception of those in xenoliths NFR1119B and NMC1302B. In these xenoliths, two compositional groupings can be distinguished based on their FeO and MnO concentrations (Fig. 4a) with no corresponding differences in petrographic features. The grouping with lower FeO and MnO contents has 10.0–10.6 wt.% FeO and 0.08–0.17 wt.% MnO in NFR1119B, and 11.5–13.1 wt.% FeO and 0.13–0.20 wt.% MnO in NMC1302B, respectively. On the other hand, olivines with higher FeO and MnO contents contain 13.0–13.8 wt.% and 15.4–15.9 wt.% FeO and 0.19–0.24 wt.% and 0.21–0.25 wt.% MnO, respectively (Fig. 4a). FeO shows a positive correlation with MnO content in all wehrlites, except for xenoliths NFK1110 and NFK1137A (Fig. 3a). The minimum (0.83 in NFK1110) and maximum (0.88 in NFR1119B) Mg# ($=Mg/(Mg + Fe^T)$) are both lower than the average Phanerozoic mantle Mg# of 0.90–0.91 (e.g., Gaul et al., 2000). The Mg# shows positive correlation with NiO and negative correlation with MnO (Supplementary Fig. 2). No correlation between the Mg# and olivine modal content is observed. Furthermore, there is no systematic difference between olivines in olivine-rich patches and those in clinopyroxene-rich patches.

Clinopyroxenes, which are dominantly diopsides (Morimoto, 1988), have highly variable chemistry represented by patchy inhomogeneities not only between xenoliths (Table 3; Supplementary Table 2), but also within a single xenolith. In the whole series, $Al_2O_3$, $TiO_2$ and CaO correlate positively with each other and range of 2.11–8.53 wt.%, 0.16–1.64 wt.% and 18.6–23.3 wt.%, respectively (Fig. 3b). This range is similar to the range observed within xenolith NME1129D, where the concentrations range of 3.45–8.53 wt.% ($Al_2O_3$), 0.37–1.64 wt.% ($TiO_2$) and 19.2–21.2 wt.% (CaO) (Fig. 4b). In contrast, $Al_2O_3$, $TiO_2$ and CaO correlate negatively with MgO and $SiO_2$. FeO shows no correlation with other basaltic elements ($Al_2O_3$, $TiO_2$, CaO, $Na_2O$). The Mg# varies widely among the xenoliths. The lowest value is observed in xenolith NMM1114 (0.84), whereas the highest value occurs in xenolith NFR1119B (0.90) (Table 3). Neither the textural position (olivine- or clinopyroxene-rich patch) nor the habit ('finger-like' or tabular) of clinopyroxenes shows any relationship with their composition.

Orthopyroxenes, which are enstatites (Morimoto, 1988), show no notable compositional variations within individual xenoliths. In contrast, significant compositional differences are observed among the different xenoliths (Table 4; Supplementary Table 3). The FeO and MnO contents show positive correlation and vary between 5.85 wt.% and 10.1 wt.% and 0.08–0.33 wt.%, respectively, for the whole series (Fig. 3c). The Mg# in orthopyroxene ranges between 0.85 (NTB1120) and 0.91 (NFR1119B). The textural position and orthopyroxene geochemistry show no correlation. The average CaO concentration is significantly higher in clinopyroxene-hosted orthopyroxenes (0.76–2.21 wt.%, with an average of 1.33 wt.%) compared to those hosted in olivine (0.74–1.15 wt.%, with an average of 0.87 wt.%) (Fig. 5a; Table 4), however, CaO shows no correlation with FeO.

Spinel composition is either homogeneous (in xenoliths NTB1109, NFK1110, NFK1137A, NMM1114) or variable (in xenoliths NTB1120, NFR1117A, NFR1119B, NMC1302B, NMC1343, NMM1129, NME1110, NME1129D) within xenoliths. FeO, $TiO_2$ and MnO concentrations show wide ranges (16.2–26.1 wt.%, 0.26–1.18 wt.% and 0.09–0.31 wt.%, respectively) (Table 5; Supplementary Table 4), and correlate positively with one another (Fig. 3d). The minimum Mg# in spinel is 0.65 in xenolith NTB1120, whereas the maximum Mg# is 0.73 in xenolith NMM1114. The Cr# ranges of 0.13–0.32. Xenolith NFK1110 shows the minimum Cr# value, and this xenolith also shows the minimum olivine Mg# (Table 2). The maximum Cr# of spinel is observed in xenolith NFR1119B, which also has the highest Mg# for all silicates (Tables 2–4). The spinel composition shows no correlation with respect to the olivine- or clinopyroxene-rich textural position.

**Table 2**
Major element compositions (in wt.%) of olivine in studied xenoliths.

| OLIVINE | | | | | | | | | |
|---|---|---|---|---|---|---|---|---|---|
| Sample | n | $SiO_2$ | FeO[a] | MnO | MgO | CaO | NiO | Total | Mg# |
| NTB1109 | 7 | 40.6 ± 0.19 | 12.3 ± 0.58 | 0.17 ± 0.02 | 47.4 ± 0.45 | 0.20 ± 0.03 | 0.31 ± 0.05 | 100.98 | 0.87 |
| NTB1120 | 29 | 39.3 ± 0.29 | 15.6 ± 0.68 | 0.27 ± 0.03 | 45.1 ± 0.53 | 0.17 ± 0.03 | 0.29 ± 0.03 | 100.73 | 0.84 |
| NFK1110 | 10 | 39.4 ± 0.15 | 16.6 ± 0.36 | 0.28 ± 0.02 | 44.1 ± 0.38 | 0.17 ± 0.02 | 0.28 ± 0.03 | 100.83 | 0.83 |
| NFK1137A | 10 | 39.8 ± 0.28 | 14.0 ± 0.65 | 0.20 ± 0.02 | 46.5 ± 0.63 | 0.19 ± 0.02 | 0.20 ± 0.05 | 100.89 | 0.86 |
| NFR1117A | 14 | 39.8 ± 0.57 | 14.3 ± 0.73 | 0.23 ± 0.03 | 46.3 ± 0.59 | 0.16 ± 0.07 | 0.28 ± 0.02 | 101.07 | 0.85 |
| NFR1119B | 16 | 40.3 ± 0.43 | 11.4 ± 1.53 | 0.16 ± 0.05 | 48.7 ± 1.28 | 0.15 ± 0.03 | 0.33 ± 0.05 | 101.04 | 0.88 |
| NMC1302B | 15 | 39.9 ± 0.38 | 12.7 ± 1.61 | 0.19 ± 0.03 | 48.0 ± 1.30 | 0.10 ± 0.03 | 0.34 ± 0.04 | 101.23 | 0.87 |
| NMC1343 | 11 | 40.9 ± 0.41 | 11.7 ± 0.22 | 0.20 ± 0.03 | 47.8 ± 0.26 | 0.12 ± 0.01 | 0.32 ± 0.05 | 101.04 | 0.88 |
| NMM1114 | 12 | 39.8 ± 0.23 | 14.1 ± 0.24 | 0.22 ± 0.03 | 46.2 ± 0.37 | 0.14 ± 0.02 | 0.25 ± 0.04 | 100.71 | 0.85 |
| NMM1129 | 13 | 39.1 ± 0.23 | 16.0 ± 0.25 | 0.26 ± 0.03 | 44.6 ± 0.24 | 0.15 ± 0.02 | 0.27 ± 0.02 | 100.38 | 0.83 |
| NME1110 | 9 | 40.0 ± 0.18 | 13.3 ± 0.48 | 0.20 ± 0.03 | 46.8 ± 0.36 | 0.16 ± 0.02 | 0.32 ± 0.04 | 100.78 | 0.86 |
| NME1129D | 12 | 40.1 ± 0.22 | 14.0 ± 0.68 | 0.20 ± 0.03 | 46.3 ± 0.32 | 0.18 ± 0.01 | 0.22 ± 0.05 | 101.00 | 0.86 |

n–number of analyses.
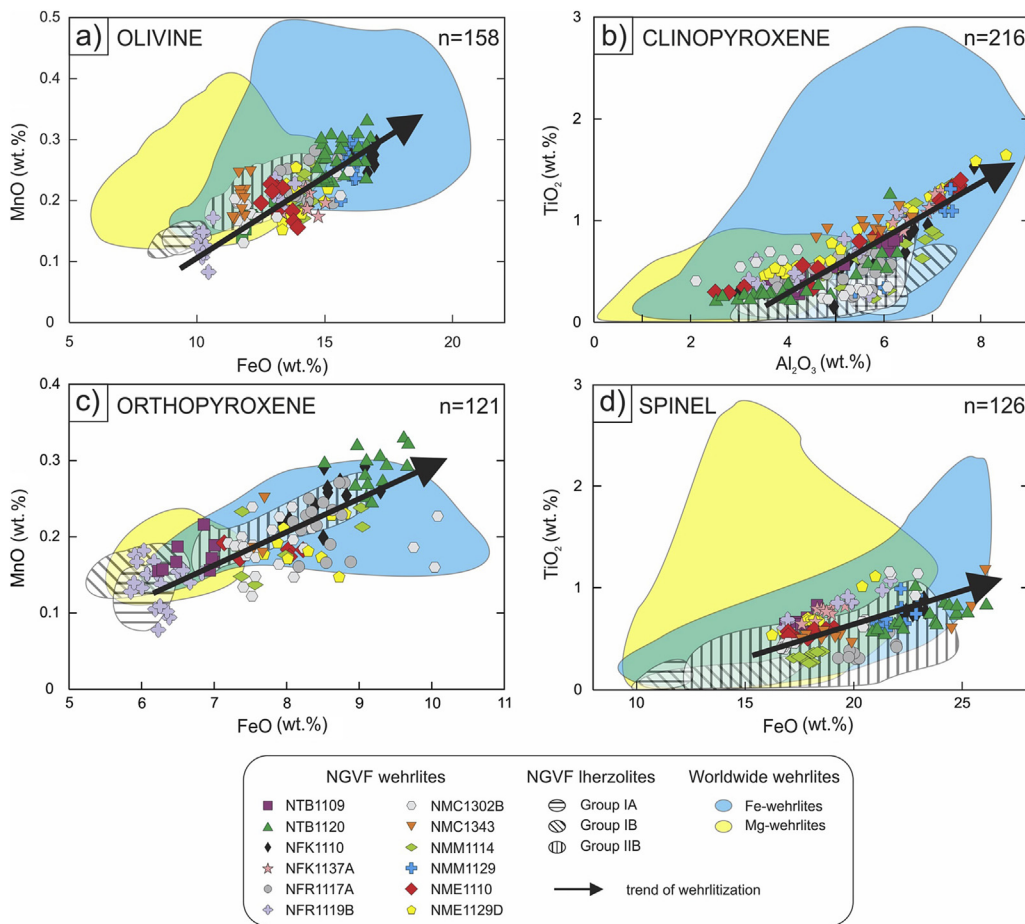
[a] total iron expressed as FeO.

**Fig. 3.** Major element composition of the NGVF wehrlite xenoliths. The chemical variation diagrams shown are: **(a)** FeO vs. MnO in olivine; **(b)** $Al_2O_3$ vs. $TiO_2$ in clinopyroxene; **(c)** FeO vs. MnO in orthopyroxene; **(d)** FeO vs. $TiO_2$ in spinel. The different NGVF lherzolite groups are from Liptai et al. (2017). The reference Fe-wehrlites are based on: Zinngrebe and Foley (1995); Xu et al. (1996); Peslier et al. (2002); Rivalenti et al. (2004); Ionov et al. (2005); Shaw et al. (2005, 2018); Raffone et al. (2009); Xiao et al. (2010); Zhang et al. (2010). The reference Mg-wehrlites are based on: Yaxley et al. (1991, 1998); Hauri et al. (1993); Xu et al. (1996); Coltorti et al. (1999); Neumann et al. (2002); Raffone et al. (2009); Scott et al. (2014).
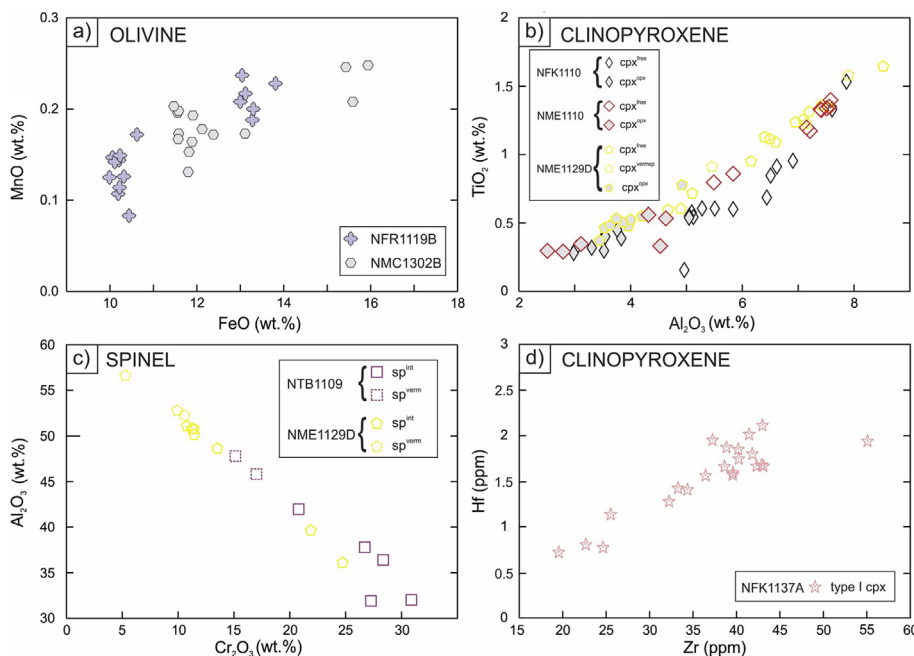


**Fig. 4.** Geochemical data for individual xenoliths, including phases that occur in different textural settings. **(a)** FeO vs. MnO in olivine; **(b)** $Al_2O_3$ vs. $TiO_2$ in clinopyroxene; **(c)** $Cr_2O_3$ vs. $Al_2O_3$ in spinel; **(d)** Zr vs. Hf in clinopyroxene. ($cpx^{free}$– vermicular spinel and orthopyroxene free clinopyroxenes; $cpx^{vermsp}$–clinopyroxenes hosting vermicular spinel; $cpx^{opx}$– clinopyroxenes hosting orthopyroxene; $sp^{int}$–interstitial spinels; $sp^{verm}$–vermicular spinel; type I cpx–clinopyroxenes with convex upward REY patterns).

## 7. Trace element geochemistry

Clinopyroxene trace element compositions (Table 6; Supplementary Table 5) show uniform multi-element patterns, having low concentrations of highly incompatible (Th, U, Nb, Ta, Pb) and some compatible elements (Co, Ni) (Fig. 6). The Hf and Zr compositions show negative anomalies and have slightly higher concentrations compared to the primitive mantle (McDonough and Sun, 1995). The highest average

**Table 3**
Major element compositions (in wt.%) of clinopyroxene in studied xenoliths.

| CLINOPYROXENE | | | | | | | | | | | | |
|---|---|---|---|---|---|---|---|---|---|---|---|---|
| Sample | Textural position | n | SiO$_2$ | TiO$_2$ | Al$_2$O$_3$ | Cr$_2$O$_3$ | FeO[a] | MnO | MgO | CaO | Na$_2$O | Total | Mg# |
| NTB1109 | cpx$^{free}$ | 5 | 51.2 ± 1.49 | 0.64 ± 0.33 | 5.44 ± 1.13 | 1.27 ± 0.34 | 3.71 ± 0.42 | 0.12 ± 0.03 | 16.1 ± 0.91 | 20.4 ± 0.57 | 1.01 ± 0.09 | 99.87 | 0.88 |
| | cpx$^{vermsp}$ | 5 | 51.3 ± 0.57 | 0.68 ± 0.12 | 5.70 ± 0.60 | 1.37 ± 0.25 | 3.99 ± 0.14 | 0.11 ± 0.02 | 16.0 ± 0.41 | 20.3 ± 0.41 | 0.94 ± 0.07 | 100.43 | 0.88 |
| | cpx$^{opx}$ | 8 | 52.1 ± 0.26 | 0.39 ± 0.07 | 4.11 ± 0.28 | 1.34 ± 0.17 | 3.47 ± 0.13 | 0.10 ± 0.02 | 17.5 ± 0.31 | 19.9 ± 0.27 | 1.03 ± 0.08 | 99.81 | 0.90 |
| NTB1120 | cpx$^{free}$ | 5 | 49.5 ± 0.63 | 0.76 ± 0.29 | 5.91 ± 0.20 | 0.89 ± 0.12 | 4.52 ± 0.17 | 0.11 ± 0.03 | 15.0 ± 0.37 | 21.4 ± 1.08 | 0.90 ± 0.25 | 99.04 | 0.85 |
| | cpx$^{vermsp}$ | 7 | 50.8 ± 1.01 | 0.38 ± 0.18 | 4.98 ± 0.90 | 1.18 ± 0.33 | 4.86 ± 0.53 | 0.16 ± 0.03 | 15.5 ± 0.57 | 20.3 ± 0.34 | 1.25 ± 0.27 | 99.33 | 0.85 |
| | cpx$^{opx}$ | 15 | 52.2 ± 0.44 | 0.28 ± 0.05 | 3.48 ± 0.55 | 1.00 ± 0.12 | 4.90 ± 0.31 | 0.20 ± 0.04 | 16.7 ± 0.42 | 19.7 ± 0.48 | 1.14 ± 0.08 | 99.53 | 0.86 |
| NFK1110 | cpx$^{free}$ | 12 | 50.0 ± 0.96 | 0.78 ± 0.37 | 6.15 ± 1.00 | 0.79 ± 0.22 | 4.99 ± 0.65 | 0.13 ± 0.03 | 15.0 ± 0.72 | 20.6 ± 0.26 | 0.98 ± 0.05 | 99.41 | 0.84 |
| | cpx$^{opx}$ | 11 | 52.0 ± 0.74 | 0.41 ± 0.10 | 3.81 ± 0.72 | 1.13 ± 0.14 | 4.72 ± 0.34 | 0.15 ± 0.03 | 16.6 ± 0.57 | 20.0 ± 0.30 | 1.05 ± 0.05 | 99.85 | 0.86 |
| NFK1137A | cpx$^{free}$ | 2 | 49.0 ± 0.11 | 1.13 ± 0.01 | 7.11 ± 0.01 | 0.98 ± 0.09 | 3.81 ± 0.01 | 0.11 ± 0.02 | 15.0 ± 0.14 | 21.7 ± 0.13 | 0.71 ± 0.01 | 99.53 | 0.87 |
| | cpx$^{vermsp}$ | 8 | 49.3 ± 0.57 | 1.04 ± 0.19 | 6.59 ± 0.55 | 1.02 ± 0.19 | 3.88 ± 0.27 | 0.09 ± 0.03 | 15.2 ± 0.47 | 21.5 ± 0.33 | 0.80 ± 0.06 | 99.34 | 0.87 |
| NFR1117A | cpx$^{free}$ | 17 | 50.9 ± 0.57 | 0.50 ± 0.14 | 5.39 ± 0.57 | 0.97 ± 0.24 | 4.25 ± 0.45 | 0.12 ± 0.02 | 15.7 ± 0.31 | 20.7 ± 0.38 | 1.08 ± 0.09 | 99.61 | 0.87 |
| | cpx$^{opx}$ | 15 | 52.4 ± 0.54 | 0.36 ± 0.05 | 3.74 ± 0.37 | 1.18 ± 0.18 | 4.41 ± 0.38 | 0.13 ± 0.02 | 16.7 ± 0.40 | 19.9 ± 0.38 | 1.10 ± 0.05 | 99.90 | 0.87 |
| NFR1119B | cpx$^{free}$ | 9 | 50.8 ± 0.79 | 0.67 ± 0.32 | 5.74 ± 0.39 | 1.22 ± 0.16 | 3.41 ± 0.70 | 0.10 ± 0.01 | 16.0 ± 0.37 | 20.6 ± 0.32 | 1.11 ± 0.18 | 99.67 | 0.89 |
| | cpx$^{opx}$ | 8 | 52.4 ± 0.50 | 0.42 ± 0.10 | 3.67 ± 0.44 | 1.32 ± 0.19 | 3.38 ± 0.38 | 0.12 ± 0.02 | 17.5 ± 0.57 | 20.2 ± 0.99 | 0.99 ± 0.15 | 99.95 | 0.90 |
| NMC1302B | cpx$^{free}$ | 9 | 51.3 ± 0.32 | 0.29 ± 0.04 | 5.33 ± 0.42 | 0.85 ± 0.10 | 3.40 ± 0.06 | 0.11 ± 0.03 | 16.2 ± 0.21 | 21.5 ± 0.08 | 0.95 ± 0.04 | 99.98 | 0.89 |
| | cpx$^{opx}$ | 6 | 52.2 ± 0.66 | 0.59 ± 0.11 | 3.38 ± 0.74 | 1.08 ± 0.09 | 4.55 ± 0.14 | 0.16 ± 0.03 | 17.5 ± 0.62 | 19.3 ± 0.32 | 0.97 ± 0.09 | 99.77 | 0.87 |
| NMC1343 | cpx$^{free}$ | 10 | 51.3 ± 0.45 | 0.96 ± 0.10 | 5.68 ± 0.60 | 1.16 ± 0.13 | 3.35 ± 0.34 | 0.08 ± 0.04 | 15.2 ± 0.58 | 21.8 ± 1.06 | 0.93 ± 0.27 | 100.49 | 0.89 |
| NMM1114 | cpx$^{free}$ | 13 | 50.3 ± 1.11 | 0.73 ± 0.36 | 6.48 ± 0.68 | 0.86 ± 0.30 | 3.95 ± 0.39 | 0.11 ± 0.02 | 15.4 ± 0.54 | 20.7 ± 0.79 | 1.09 ± 0.24 | 99.62 | 0.87 |
| | cpx$^{opx}$ | 6 | 51.6 ± 0.78 | 0.50 ± 0.14 | 4.76 ± 0.85 | 0.95 ± 0.15 | 4.22 ± 0.18 | 0.13 ± 0.04 | 16.9 ± 0.61 | 19.8 ± 0.67 | 1.02 ± 0.03 | 99.53 | 0.87 |
| NMM1129 | cpx$^{free}$ | 6 | 49.3 ± 1.14 | 0.83 ± 0.47 | 6.69 ± 0.93 | 0.64 ± 0.08 | 4.63 ± 0.94 | 0.12 ± 0.03 | 14.9 ± 0.78 | 21.0 ± 0.30 | 0.97 ± 0.04 | 99.06 | 0.85 |
| NME1110 | cpx$^{free}$ | 9 | 49.3 ± 0.65 | 1.20 ± 0.22 | 7.02 ± 0.79 | 0.86 ± 0.21 | 3.94 ± 0.30 | 0.09 ± 0.03 | 15.0 ± 0.41 | 21.4 ± 0.08 | 0.91 ± 0.04 | 99.67 | 0.87 |
| | cpx$^{opx}$ | 6 | 52.3 ± 0.50 | 0.39 ± 0.12 | 3.65 ± 0.95 | 1.00 ± 0.19 | 4.12 ± 0.39 | 0.10 ± 0.02 | 17.2 ± 0.60 | 20.3 ± 0.71 | 0.89 ± 0.03 | 99.97 | 0.88 |
| NME1129D | cpx$^{free}$ | 13 | 49.8 ± 1.05 | 1.10 ± 0.31 | 6.54 ± 1.12 | 0.84 ± 0.23 | 4.37 ± 0.29 | 0.11 ± 0.03 | 15.1 ± 0.64 | 20.8 ± 0.24 | 0.94 ± 0.05 | 99.62 | 0.86 |
| | cpx$^{vermsp}$ | 3 | 49.3 ± 1.25 | 1.24 ± 0.33 | 6.83 ± 1.25 | 0.96 ± 0.36 | 4.35 ± 0.16 | 0.10 ± 0.01 | 14.9 ± 0.63 | 20.8 ± 0.32 | 0.94 ± 0.04 | 99.43 | 0.86 |
| | cpx$^{opx}$ | 9 | 52.2 ± 0.63 | 0.52 ± 0.11 | 3.92 ± 0.44 | 1.12 ± 0.12 | 4.26 ± 0.40 | 0.13 ± 0.02 | 16.9 ± 0.59 | 20.2 ± 0.60 | 0.93 ± 0.07 | 100.18 | 0.88 |

n–number of analyses.
cpx$^{free}$–clinopyroxene without orthopyroxene remnants and vermicular spinel.
cpx$^{opx}$–clinopyroxene hosting orthopyroxene.
cpx$^{vermsp}$–clinopyroxene hosting vermicular spinel.
[a] total iron expressed as FeO.

Hf and Zr concentrations are found in xenoliths NFK1137A (1.55 ppm) and NMM1129 (38.7 ppm), respectively, whereas the lowest average values are found in xenolith NTB1109 (0.3 ppm and 9.10 ppm, respectively) (Fig. 6). Concentrations of Ti are variable with respect to their neighboring elements (Fig. 6). Beside these common features, there are some additional trace element characteristics in the REY patterns (Fig. 7) not only between xenoliths but within xenoliths as well. Three different clinopyroxene groups, type I, type II and type III, can be distinguished based on the REY patterns.

All wehrlites, with the exception of xenolith NMC1302B, display convex upward REY patterns with maximum values mostly at Nd, and rarely at Ce in xenolith NTB1120 (Fig. 7a). Samples displaying this behavior will hereafter be referred to as type I. The normalized LREE and HREE concentrations are 3–8 times and 2–3 times higher, respectively, compared to primitive mantle (PM; McDonough and Sun, 1995). The most common REY pattern shows an average Nd$_N$/Yb$_N$ (normalized to the PM of McDonough and Sun (1995)) that is higher than 1.7 (1.73–3.58), with the exception of clinopyroxenes hosted in vermicular spinel in xenolith NTB1109 (1.53) and in xenolith NME1110 (1.02) (Table 6). Type I clinopyroxenes appear exclusively in xenoliths NTB1109, NTB1120, NFK1137A, NMM1114 and NME1129D.

Type II clinopyroxenes show a rather flat REY pattern with an average

**Table 4**
Major element compositions (in wt.%) of orthopyroxene in studied xenoliths.

| ORTHOPYROXENE | | | | | | | | | | | |
|---|---|---|---|---|---|---|---|---|---|---|---|
| Sample | Textural position | n | SiO$_2$ | TiO$_2$ | Al$_2$O$_3$ | Cr$_2$O$_3$ | FeO[a] | MnO | MgO | CaO | Total | Mg# |
| NTB1109 | opx$^{cpx}$ | 9 | 55.7 ± 0.21 | 0.12 ± 0.01 | 2.42 ± 0.23 | 0.56 ± 0.04 | 6.70 ± 0.32 | 0.17 ± 0.02 | 33.5 ± 0.40 | 1.38 ± 0.09 | 100.69 | 0.90 |
| NTB1120 | opx$^{cpx}$ | 14 | 55.1 ± 0.34 | 0.11 ± 0.02 | 2.08 ± 0.48 | 0.47 ± 0.12 | 9.21 ± 0.31 | 0.29 ± 0.03 | 31.6 ± 0.20 | 1.23 ± 0.09 | 100.32 | 0.86 |
| NFK1110 | opx$^{cpx}$ | 12 | 55.2 ± 0.33 | 0.13 ± 0.03 | 2.48 ± 0.44 | 0.42 ± 0.07 | 8.57 ± 0.39 | 0.25 ± 0.03 | 32.0 ± 0.36 | 1.37 ± 0.06 | 100.48 | 0.87 |
| NFR1117A | opx$^{cpx}$ | 12 | 55.5 ± 0.27 | 0.15 ± 0.03 | 2.45 ± 0.16 | 0.50 ± 0.07 | 8.47 ± 0.28 | 0.22 ± 0.03 | 32.5 ± 0.34 | 1.28 ± 0.16 | 101.25 | 0.87 |
| | opx$^{ol}$ | 3 | 54.7 ± 0.04 | 0.06 ± 0.01 | 3.89 ± 0.03 | 0.35 ± 0.05 | 8.55 ± 0.05 | 0.20 ± 0.04 | 32.3 ± 0.09 | 0.80 ± 0.03 | 100.98 | 0.87 |
| NFR1119B | opx$^{cpx}$ | 14 | 55.8 ± 0.19 | 0.13 ± 0.03 | 2.44 ± 0.27 | 0.60 ± 0.05 | 6.15 ± 0.30 | 0.15 ± 0.03 | 33.8 ± 0.33 | 1.37 ± 0.07 | 100.57 | 0.91 |
| | opx$^{ol}$ | 8 | 55.4 ± 0.15 | 0.07 ± 0.03 | 3.39 ± 0.23 | 0.47 ± 0.08 | 6.37 ± 0.15 | 0.13 ± 0.03 | 33.8 ± 0.13 | 0.84 ± 0.15 | 100.72 | 0.90 |
| NMC1302B | opx$^{cpx}$ | 11 | 54.8 ± 0.42 | 0.16 ± 0.07 | 3.14 ± 0.65 | 0.49 ± 0.06 | 7.89 ± 0.32 | 0.19 ± 0.03 | 32.6 ± 0.42 | 1.20 ± 0.25 | 100.64 | 0.88 |
| | opx$^{ol}$ | 14 | 54.6 ± 0.41 | 0.07 ± 0.02 | 3.57 ± 0.09 | 0.41 ± 0.05 | 7.98 ± 1.08 | 0.18 ± 0.03 | 32.7 ± 0.79 | 0.86 ± 0.05 | 100.56 | 0.88 |
| NMC1343 | opx$^{ol}$ | 3 | 55.2 ± 0.09 | 0.10 ± 0.01 | 3.68 ± 0.05 | 0.39 ± 0.05 | 7.64 ± 0.08 | 0.21 ± 0.04 | 32.4 ± 0.18 | 0.91 ± 0.04 | 100.76 | 0.88 |
| NMM1114 | opx$^{cpx}$ | 5 | 54.9 ± 0.54 | 0.12 ± 0.06 | 3.93 ± 0.68 | 0.32 ± 0.06 | 7.54 ± 0.26 | 0.18 ± 0.04 | 32.2 ± 0.20 | 1.16 ± 0.62 | 100.47 | 0.88 |
| | opx$^{ol}$ | 2 | 54.4 ± 0.08 | 0.09 ± 0.02 | 3.87 ± 0.01 | 0.27 ± 0.04 | 9.04 ± 0.01 | 0.23 ± 0.02 | 31.4 ± 0.02 | 1.01 ± 0.04 | 100.57 | 0.86 |
| NME1110 | opx$^{cpx}$ | 5 | 55.3 ± 0.31 | 0.17 ± 0.03 | 2.27 ± 0.22 | 0.46 ± 0.15 | 7.76 ± 0.48 | 0.18 ± 0.01 | 32.8 ± 0.50 | 1.48 ± 0.06 | 100.57 | 0.88 |
| NME1129D | opx$^{cpx}$ | 9 | 55.4 ± 0.46 | 0.21 ± 0.03 | 2.83 ± 0.85 | 0.38 ± 0.08 | 8.28 ± 0.41 | 0.19 ± 0.03 | 32.1 ± 0.63 | 1.52 ± 0.09 | 101.15 | 0.87 |

n–number of analyses.
opx$^{cpx}$–orthopyroxene in clinopyroxene.
opx$^{ol}$–orthopyroxene in olivine.
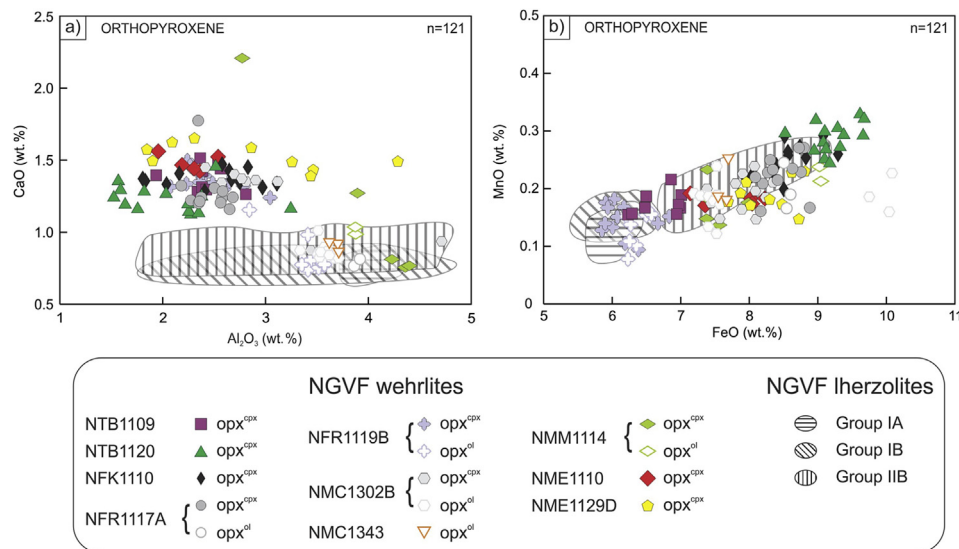[a] total iron expressed as FeO.

**Fig. 5.** (a) Al₂O₃ vs. CaO and (b) FeO vs. MnO relationships in orthopyroxene with respect to their textural position (opx$^{cpx}$– orthopyroxenes hosted by clinopyroxenes; opx$^{ol}$– orthopyroxenes hosted by olivines). The different NGVF lherzolite groups are from Liptai et al. (2017).

**Table 5**
Major element compositions (in wt.%) of spinel in studied xenoliths.

| SPINEL | | | | | | | | | | | | |
|---|---|---|---|---|---|---|---|---|---|---|---|---|
| Sample | Textural position | n | TiO₂ | Al₂O₃ | Cr₂O₃ | FeO[a] | MnO | NiO | MgO | Total | Mg# | Cr# |
| NTB1109 | sp$^{int}$ | 2 | 0.65 ± 0.02 | 46.8 ± 1.40 | 16.1 ± 1.33 | 17.4 ± 0.17 | 0.20 ± 0.01 | 0.28 ± 0.01 | 18.0 ± 0.41 | 99.38 | 0.73 | 0.19 |
| | sp$^{verm}$ | 5 | 0.69 ± 0.08 | 36.0 ± 4.23 | 26.8 ± 3.72 | 17.8 ± 0.57 | 0.17 ± 0.02 | 0.25 ± 0.03 | 16.4 ± 0.39 | 98.12 | 0.70 | 0.33 |
| NTB1120 | sp$^{int}$ | 11 | 0.65 ± 0.10 | 43.9 ± 1.24 | 16.5 ± 1.21 | 22.2 ± 1.25 | 0.24 ± 0.04 | 0.28 ± 0.03 | 15.9 ± 0.82 | 99.67 | 0.66 | 0.20 |
| | sp$^{verm}$ | 8 | 0.77 ± 0.12 | 40.2 ± 3.34 | 18.4 ± 3.11 | 24.4 ± 1.00 | 0.24 ± 0.04 | 0.27 ± 0.03 | 15.2 ± 0.56 | 99.51 | 0.64 | 0.24 |
| NFK1110 | sp$^{int}$ | 10 | 0.78 ± 0.05 | 48.4 ± 1.60 | 10.9 ± 1.98 | 22.7 ± 0.34 | 0.19 ± 0.02 | 0.32 ± 0.04 | 16.6 ± 0.22 | 99.98 | 0.67 | 0.13 |
| NFK1137A | sp$^{int}$ | 5 | 0.74 ± 0.08 | 48.3 ± 1.73 | 14.0 ± 1.27 | 18.3 ± 0.49 | 0.17 ± 0.02 | 0.23 ± 0.04 | 18.2 ± 0.36 | 99.89 | 0.73 | 0.16 |
| | sp$^{verm}$ | 4 | 0.78 ± 0.03 | 47.0 ± 0.58 | 15.0 ± 0.53 | 18.9 ± 0.44 | 0.16 ± 0.04 | 0.22 ± 0.02 | 17.9 ± 0.09 | 100.03 | 0.72 | 0.18 |
| NFR1117A | sp$^{int}$ | 9 | 0.38 ± 0.09 | 44.4 ± 0.72 | 17.2 ± 0.71 | 20.5 ± 1.03 | 0.17 ± 0.02 | 0.29 ± 0.03 | 16.8 ± 0.52 | 99.79 | 0.69 | 0.21 |
| NFR1119B | sp$^{int}$ | 9 | 0.83 ± 0.15 | 37.2 ± 2.96 | 26.0 ± 4.35 | 19.1 ± 1.86 | 0.17 ± 0.03 | 0.23 ± 0.04 | 16.3 ± 0.51 | 99.88 | 0.69 | 0.32 |
| NMC1302B | sp$^{int}$ | 14 | 0.66 ± 0.30 | 44.2 ± 3.07 | 18.7 ± 1.82 | 19.1 ± 2.53 | 0.19 ± 0.04 | 0.30 ± 0.04 | 17.0 ± 1.16 | 100.17 | 0.69 | 0.22 |
| NMC1343 | sp$^{int}$ | 11 | 0.63 ± 0.21 | 42.0 ± 4.29 | 20.7 ± 3.62 | 20.5 ± 3.18 | 0.23 ± 0.04 | 0.26 ± 0.02 | 15.8 ± 1.65 | 100.17 | 0.66 | 0.25 |
| NMM1114 | sp$^{int}$ | 9 | 0.32 ± 0.04 | 51.0 ± 1.79 | 12.0 ± 1.93 | 17.9 ± 0.41 | 0.16 ± 0.03 | 0.26 ± 0.03 | 18.4 ± 0.33 | 100.12 | 0.73 | 0.14 |
| NMM1129 | sp$^{int}$ | 10 | 0.73 ± 0.14 | 48.2 ± 2.28 | 11.8 ± 2.03 | 21.9 ± 0.68 | 0.19 ± 0.03 | 0.29 ± 0.04 | 16.5 ± 0.56 | 99.59 | 0.67 | 0.14 |
| NME1110 | sp$^{int}$ | 9 | 0.54 ± 0.04 | 48.7 ± 1.07 | 14.4 ± 1.19 | 17.7 ± 0.77 | 0.15 ± 0.02 | 0.31 ± 0.03 | 18.2 ± 0.40 | 100.02 | 0.73 | 0.17 |
| NME1129D | sp$^{int}$ | 3 | 0.56 ± 0.02 | 54.0 ± 2.61 | 8.59 ± 2.89 | 16.5 ± 0.30 | 0.12 ± 0.03 | 0.31 ± 0.01 | 19.5 ± 0.40 | 99.64 | 0.76 | 0.10 |
| | sp$^{verm}$ | 4 | 0.87 ± 0.22 | 43.8 ± 7.04 | 17.9 ± 6.43 | 19.2 ± 1.64 | 0.17 ± 0.03 | 0.21 ± 0.05 | 17.4 ± 1.28 | 99.52 | 0.71 | 0.22 |
| | sp$^{incl}$ | 3 | 0.68 ± 0.01 | 50.7 ± 0.47 | 11.2 ± 0.33 | 18.2 ± 0.19 | 0.15 ± 0.03 | 0.28 ± 0.04 | 18.4 ± 0.03 | 99.53 | 0.73 | 0.13 |

n – number of analyses.
sp$^{int}$–interstitial spinel.
sp$^{verm}$ –vermicular spinel.
sp$^{incl}$–spinel inclusion in cpx.
[a] total iron expressed as FeO.

Nd$_N$/Yb$_N$ ratio lower than 1.7 (0.87–1.54) (Table 6). Both the normalized LREE and HREE data are 2–5 times higher than the PM value (Fig. 7b) (McDonough and Sun, 1995). Type II clinopyroxenes are less common compared to type I clinopyroxenes, although this is the only type present in NMC1302B xenolith. This pattern is also characteristic for xenoliths NFR1117A, NMM1129 and NME1110.

Four xenoliths (NFK1110, NFR1119B, NMC1343, NME1110) display REY patterns of clinopyroxenes that are unlike the type I or type II groups, and hence are referred to as type III. Type III clinopyroxenes have flat HREE pattern, but variable LREE values. Three out of the four xenoliths (NFR1119B, NMC1343, NME1110) show a depletion in LREE. In contrast, in xenolith NFK1110, type III clinopyroxenes show a gradual LREE enrichment (Fig. 7c) with 4–6 times higher values compared to the PM (McDonough and Sun, 1995). Similar to type II clinopyroxenes, type III clinopyroxenes also show low Nd$_N$/Yb$_N$ ratios (0.67–1.61) (Table 6).

Neither the average ΣREE value (16–76 ppm), nor the average La$_N$/Lu$_N$ ratio (0.3–4.2), shows any relationship with the aforementioned grouping. The minimum values for ΣREE and La$_N$/Lu$_N$ ratio are derived from type III clinopyroxenes in xenoliths NFR1119B and NME1110, respectively (Table 6). In contrast, the maximum values were found in the type I and type II clinopyroxenes of two different samples, namely xenolith NMM1129 and NFR1117A, respectively (Table 6). In general, the higher the ΣREE content, the higher the La$_N$/Lu$_N$ ratio.

## 8. Whole rock geochemistry

All details regarding the whole rock compositions of wehrlite xenoliths can be found in the Supplementary Text. The whole rock data are summarized in Supplementary Table 6 and shown graphically in Supplementary Figs. 3 and 4.

## 9. Discussion

### 9.1. Examination of the processes leading to wehrlite formation

Petrographic observations, (e.g., breakdown of amphiboles and reaction coronas at the contact between host basalt and xenolith; see Supplementary Fig. 1c and d; the lack of any relationship between the size and position of orthopyroxene remnants and their distance from the host basalt), and geochemical features (e.g., rock-forming minerals showing compositional zoning only at the margins of xenoliths; Supplementary Fig. 1c and d) indicate that the host basaltic melt only interacted with the outer portions of the xenoliths. Therefore, the host basalt could not have been responsible for the wehrlitization process observed in the interiors of xenoliths, hence the clinopyroxene-rich lithology must have formed before the xenolith was entrained in the basalt melt.

Orthopyroxenes occurring within clinopyroxenes show irregular shapes characteristic of relict crystals (Fig. 2g). These crystals are considered to have been involved in wehrlite formation and were partially replaced by newly formed clinopyroxenes (Fig. 2g). This petrographic observation clearly demonstrates that wehrlite is a product of a reaction between a metasomatic agent and the peridotite wall rock. The presence of orthopyroxene indicates that the wehrlite precursor lithology contained orthopyroxene, and thus was likely a lherzolite, characteristic of the upper mantle in the study area (Liptai et al., 2017).

The appearance of orthopyroxenes in clinopyroxene cores (Fig. 2g) also reveals that the metasomatic agent migrated along grain boundaries. The moderate LREE/HREE fractionation (La$_N$/Lu$_N$: 0.7–3.6; Fig. 7) and the dominant convex upward trace element patterns of type I clinopyroxene (Fig. 7a) in wehrlite xenoliths indicate that the metasomatic process was controlled by diffusion (Navon and Stolper, 1987; Bodinier et al., 1990). According to Bodinier et al. (1990), diffusion-controlled metasomatism takes place in close proximity to migration pathways of the metasomatic agent, which is supported by our petrographic observations including the entirely new mineral assemblage (Fig. 2a) and metasomatic reactions related to both pyroxenes (Fig. 2g) and spinel (Fig. 2f).

Based on their elevated basaltic element (Fe, Mn, Ti, Ca, Al) contents compared to those of Group IA, IB and IIB lherzolites of Liptai et al. (2017) (Group IIA lherzolites are missing in central NGVF) (Fig. 3), olivines, clinopyroxenes and spinels were all affected by the metasomatism, regardless to their textural position. This is strong geochemical evidence for a common and extensive metasomatic event in the upper mantle beneath the NGVF. The proposed lherzolite precursor is also confirmed by the geochemistry of the wehrlitization trends, which always indicate Group IA and Group IB lherzolite fields (Liptai et al., 2017) as the starting major element compositions for olivine, pyroxenes and spinel (Fig. 3; Supplementary Fig. 2). The wehrlitization trends partially overlap with Group IIB lherzolites of Liptai et al. (2017), however some wehrlite xenoliths have higher basaltic element (Fe, Mn, Ti, Ca, Al) compositions than those of Liptai et al. (2017) (Fig. 3; Supplementary Fig. 2). This observation supports the interpretation of Liptai et al. (2017) that Group IIB lherzolites were formed during the same event as the wehrlites, as explained below. The convex upward REY pattern shown by type I clinopyroxenes in wehrlites (Fig. 7a) agrees well with that of Group IIB NGVF lherzolites (Fig. 7d), further supporting their common origin. The flat REY distribution in type II clinopyroxenes of wehrlite xenoliths (Fig. 7b), as well as the LREE-enriched and LREE-depleted patterns of type III clinopyroxenes of wehrlite xenoliths (Fig. 7c), are also similar to the Group IIB, Group IB and Group IA lherzolites (Fig. 7d). Interestingly, a restricted number of clinopyroxene grains in wehrlites that show trace element patterns similar to Group IA xenoliths of Liptai et al. (2017) (Fig. 7d) may represent preserved areas remaining unaffected by metasomatism. This suggests that the last wehrlitization event has not entirely overprinted the precursor. Lower basaltic major element concentrations, e.g., in NTB1109 and NFR1119D wehrlites, compared to other wehrlites (Fig. 3) represent further evidence that some areas remained unaffected

by the metasomatic event.

### 9.2. Composition and chemical evolution of the metasomatic agent

#### 9.2.1. Nature of the metasomatic agent

According to previous studies on wehrlites (e.g., Rudnick et al., 1993; Zinngrebe and Foley, 1995; Yaxley et al., 1998; Coltorti et al., 1999; Peslier et al., 2002), the metasomatic agent responsible for orthopyroxene consumption and clinopyroxene formation could be either a silicate melt or a carbonate melt, forming Fe- or Mg-wehrlites, respectively. Additionally, supercritical CO$_2$–H$_2$O-rich fluids, generated by decarbonation of carbonate melts, can also cause Mg-wehrlitic metasomatism (Yaxley et al., 1991). Moreover, the metasomatic melts need not be pure silicic or carbonatic endmembers. Lee and Wyllie (1997) conducted experiments in the nephelinite-dolomite-Na$_2$CO$_3$ and nephelinite-calcite systems and proposed silicate-carbonate liquid mixing during magmatic processes at upper mantle conditions as a possible mechanism leading to the formation of 'carbonatic silicate' (e.g., Xiao et al., 2010) or 'silicic carbonate' melts (e.g., Neumann et al., 2002) depending on the dominant component.

The NGVF wehrlites contain neither carbonate phases nor apatite, which normally occur in Mg-wehrlites as a result of decarbonation processes (Yaxley et al., 1991, 1998; Hauri et al., 1993; Rudnick et al., 1993; Scott et al., 2014). This suggests that NGVF wehrlite formation is not related to carbonate melts. Furthermore, the observed 10–24 vol.% clinopyroxene mode (Table 1) is lower than the clinopyroxene content in products of carbonate-dominated metasomatism (20–40 vol.%; Gervasoni et al., 2017). The calculated low CaO/Al$_2$O$_3$ ratio (3–5.7) in clinopyroxenes (Table 3) (>5 in carbonate-dominated metasomatism; Yaxley et al., 1991) is inconsistent with carbonate-dominated metasomatism, but is characteristic of mafic melt-driven metasomatism. Similarly, the low Mg# in rock-forming silicates (0.86, 0.88, 0.87 for olivine, orthopyroxene and clinopyroxene, respectively; Tables 2–4) in the NGVF wehrlites is characteristic of mafic melt-driven metasomatism. In contrast, the high Mg# in silicates (≥0.9; Yaxley et al., 1991) is typical of carbonate-dominated metasomatism. All clinopyroxenes in NGVF wehrlites show high Ti/Eu and low La$_N$/Yb$_N$ ratios (~1100–12,000 and 0.2–3.8, respectively), which is characteristic of silicate metasomatism (Coltorti et al., 1999) (Fig. 8). Furthermore, the major element trends of NGVF wehrlites overlap with worldwide Fe-wehrlite trends, but not with Mg-wehrlite fields (Fig. 3; Supplementary Fig. 2).

The presence of silicate melt inclusions hosted by clinopyroxenes and olivines in the wehrlites suggests that the metasomatic agent is a silicate melt, without a carbonate melt contribution. The silicate melt inclusions always contain low-to-moderate density (0.17–0.57 g/cm$^3$) CO$_2$-dominated bubbles (Patkó et al., 2018). All of the observed geochemical features are consistent with a mafic silicate melt metasomatic agent (Patkó et al., 2018).

#### 9.2.2. Metasomatic melt composition

To constrain the main geochemical features of the silicate melt agent, we compared the mineral compositions of the product wehrlite and the potential precursor lherzolite xenoliths (Group IA, IB and IIB xenoliths of Liptai et al., 2017) collected from the same locations of the central NGVF (Fig. 1b). The comparison shows enrichment of Fe, Mn, Ca in olivines, Fe, Mn, and Ca enrichment in orthopyroxenes, Fe, Ti, Al, and Mn enrichment in clinopyroxenes, and Fe and Ti enrichment in spinels, compared to compositions of these phases in all lherzolite groups (Figs. 3 and 5; Supplementary Fig. 2). In contrast, the trace element characteristics of clinopyroxenes in the wehrlite and lherzolite series are similar (Figs. 6 and 7). Among the HFS elements, Ti shows a positive correlation with Nb and Ta (Fig. 9a) and with Zr and Hf (Fig. 9b) in clinopyroxenes of all wehrlites and Group IIB lherzolites. This positive correlation is significant even within single xenoliths, particularly for Zr and Hf in xenolith NFK1137A (r$^2$ = 0.89 and 0.85, respectively) (Fig. 4d).

**Table 6**
Trace element concentrations (in ppm) of clinopyroxenes in the studied xenoliths.

CLINOPYROXENE

| Sample | Textural position | REE type | n | Th | U | Nb | Ta | La | Ce | Pb | Sr | Pr | Nd | Hf | Zr | Sm | Eu |
|---|---|---|---|---|---|---|---|---|---|---|---|---|---|---|---|---|---|
| NTB1109 | cpx^free | type I | 10 | 0.02 ± 0.01 | n.d. | 0.34 ± 0.05 | 0.04 ± 0.01 | 1.90 ± 0.33 | 6.39 ± 0.80 | 0.15 ± 0.03 | 74.2 ± 6.4 | 1.04 ± 0.13 | 5.45 ± 0.78 | 0.33 ± 0.14 | 9.57 ± 3.37 | 1.50 ± 0.22 | 0.55 ± 0.01 |
| | cpx^vermsp | | 4 | 0.03 ± 0.01 | 0.01 ± 0.01 | n.d. | n.d. | 1.40 ± 0.20 | 4.82 ± 0.87 | n.d. | 64.2 ± 5.6 | 0.72 ± 0.10 | 4.11 ± 0.71 | 0.27 ± 0.07 | 6.98 ± 2.31 | 1.32 ± 0.08 | 0.46 ± 0.07 |
| | cpx^opx | | 15 | 0.03 ± 0.01 | 0.01 ± 0.01 | 0.42 ± 0.13 | 0.04 ± 0.01 | 1.88 ± 0.24 | 5.95 ± 0.82 | 0.16 ± 0.08 | 74.4 ± 4.2 | 1.00 ± 0.15 | 5.07 ± 0.66 | 0.29 ± 0.14 | 9.35 ± 3.19 | 1.47 ± 0.39 | 0.61 ± 0.12 |
| NTB1120 | cpx^free | type I | 15 | 0.04 ± 0.02 | 0.02 ± 0.01 | 0.26 ± 0.18 | 0.05 ± 0.03 | 5.10 ± 0.74 | 15.5 ± 1.6 | 0.16 ± 0.08 | 127 ± 17 | 2.38 ± 0.19 | 11.3 ± 1.1 | 0.58 ± 0.33 | 19.1 ± 8.7 | 2.73 ± 0.48 | 0.96 ± 0.14 |
| | cpx^vermsp | | 4 | 0.03 ± 0.01 | 0.02 ± 0.01 | 0.23 ± 0.05 | 0.02 ± 0.01 | 4.81 ± 0.43 | 15.8 ± 1.5 | 0.16 ± 0.08 | 113 ± 19 | 2.27 ± 0.11 | 10.9 ± 0.6 | 0.55 ± 0.19 | 18.5 ± 3.9 | 2.42 ± 0.19 | 0.97 ± 0.02 |
| | cpx^opx | | 13 | 0.04 ± 0.01 | 0.01 ± 0.01 | 0.25 ± 0.11 | 0.04 ± 0.02 | 4.67 ± 0.59 | 16.4 ± 1.0 | 0.13 ± 0.03 | 119 ± 12 | 2.48 ± 0.17 | 11.9 ± 1.1 | 0.67 ± 0.35 | 21.3 ± 7.1 | 2.71 ± 0.42 | 1.02 ± 0.09 |
| NFK1110 | cpx^free | type I | 23 | 0.05 ± 0.02 | 0.01 ± 0.01 | 0.26 ± 0.12 | 0.03 ± 0.02 | 3.26 ± 0.65 | 10.7 ± 1.6 | 0.11 ± 0.03 | 87.1 ± 4.9 | 1.76 ± 0.19 | 8.90 ± 0.97 | 0.67 ± 0.19 | 19.6 ± 4.3 | 2.31 ± 0.34 | 0.87 ± 0.11 |
| | cpx^opx | | 5 | 0.04 ± 0.02 | 0.01 ± 0.01 | 0.36 ± 0.14 | 0.05 ± 0.03 | 3.02 ± 0.62 | 10.2 ± 1.51 | 0.11 ± 0.06 | 84.3 ± 8.8 | 1.71 ± 0.23 | 8.77 ± 1.64 | 0.61 ± 0.32 | 20.0 ± 9.9 | 2.42 ± 0.48 | 0.89 ± 0.11 |
| | cpx^free | type III | 10 | 0.08 ± 0.02 | 0.02 ± 0.01 | 0.10 ± 0.05 | 0.01 ± 0.01 | 3.85 ± 0.30 | 9.41 ± 0.97 | 0.12 ± 0.02 | 74.5 ± 4.5 | 1.29 ± 0.15 | 5.69 ± 0.59 | 0.93 ± 0.12 | 24.7 ± 2.2 | 1.68 ± 0.32 | 0.61 ± 0.05 |
| NFK1137A | cpx^free | type I | 11 | 0.06 ± 0.02 | 0.02 ± 0.01 | 0.50 ± 0.11 | 0.09 ± 0.02 | 3.11 ± 0.32 | 9.83 ± 0.73 | 0.12 ± 0.01 | 75.8 ± 1.4 | 1.73 ± 0.18 | 9.45 ± 1.26 | 1.45 ± 0.43 | 35.0 ± 8.8 | 2.71 ± 0.33 | 0.93 ± 0.14 |
| | cpx^vermsp | | 11 | 0.07 ± 0.02 | 0.02 ± 0.01 | 0.52 ± 0.20 | 0.11 ± 0.04 | 3.41 ± 0.58 | 11.2 ± 1.6 | 0.09 ± 0.09 | 78.2 ± 5.3 | 1.93 ± 0.24 | 10.5 ± 1.4 | 1.66 ± 0.35 | 38.9 ± 7.3 | 3.18 ± 0.34 | 1.02 ± 0.12 |
| NFR1117A | cpx^free | type I | 12 | 0.03 ± 0.01 | 0.01 ± 0.01 | 0.26 ± 0.20 | 0.04 ± 0.03 | 2.62 ± 0.68 | 9.03 ± 2.14 | 0.11 ± 0.05 | 84.7 ± 7.7 | 1.47 ± 0.33 | 7.44 ± 1.95 | 0.44 ± 0.26 | 12.4 ± 6.3 | 1.94 ± 0.45 | 0.79 ± 0.13 |
| | cpx^opx | | 9 | 0.06 ± 0.04 | 0.01 ± 0.01 | 0.22 ± 0.19 | 0.02 ± 0.02 | 2.76 ± 0.53 | 8.63 ± 1.57 | 0.16 ± 0.05 | 78.3 ± 16.5 | 1.31 ± 0.18 | 6.33 ± 0.73 | 0.39 ± 0.16 | 11.7 ± 4.5 | 1.71 ± 0.26 | 0.68 ± 0.08 |
| | cpx^free | type II | 8 | 0.05 ± 0.03 | 0.02 ± 0.01 | 0.16 ± 0.07 | 0.01 ± 0.01 | 2.27 ± 0.59 | 7.04 ± 0.83 | 0.10 ± 0.01 | 56.8 ± 8.1 | 1.16 ± 0.13 | 6.09 ± 0.97 | 0.56 ± 0.10 | 12.1 ± 3.0 | 1.95 ± 0.31 | 0.78 ± 0.11 |
| NFR1119B | cpx^free | type III | 18 | 0.03 ± 0.01 | 0.02 ± 0.01 | 0.19 ± 0.02 | 0.04 ± 0.01 | 1.00 ± 0.32 | 3.74 ± 1.10 | 0.19 ± 0.09 | 55.1 ± 11.3 | 0.63 ± 0.17 | 3.08 ± 0.60 | 0.46 ± 0.10 | 14.4 ± 3.0 | 1.11 ± 0.21 | 0.43 ± 0.08 |
| | cpx^opx | type I | 6 | 0.03 ± 0.01 | 0.01 ± 0.01 | 0.26 ± 0.11 | 0.04 ± 0.01 | 1.88 ± 0.45 | 6.11 ± 0.83 | 0.22 ± 0.11 | 87.1 ± 15.1 | 1.00 ± 0.19 | 5.08 ± 0.84 | 0.23 ± 0.07 | 8.00 ± 3.15 | 1.40 ± 0.09 | 0.54 ± 0.09 |
| NMC1302B | cpx^free | type II | 16 | 0.05 ± 0.01 | 0.01 ± 0.01 | 0.22 ± 0.11 | 0.03 ± 0.02 | 3.06 ± 0.25 | 9.06 ± 0.57 | 0.12 ± 0.03 | 68.5 ± 5.9 | 1.36 ± 0.17 | 6.67 ± 1.35 | 0.87 ± 0.13 | 23.9 ± 2.5 | 1.90 ± 0.45 | 0.75 ± 0.13 |
| | cpx^opx | | 6 | 0.03 ± 0.02 | 0.001± 0.01 | 0.43 ± 0.31 | 0.05 ± 0.04 | 2.32 ± 0.86 | 8.33 ± 2.36 | n.d. | 74.1 ± 9.5 | 1.45 ± 0.31 | 7.49 ± 1.89 | 0.54 ± 0.36 | 14.3 ± 8.7 | 2.37 ± 0.45 | 0.94 ± 0.14 |
| NMC1343 | cpx^free | type I | 34 | 0.15 ± 0.09 | 0.05 ± 0.03 | 0.39± 0.18 | 0.06 ± 0.03 | 3.64 ± 0.77 | 10.8 ± 2.3 | 0.15 ± 0.07 | 79.7 ± 15.0 | 1.73 ± 0.41 | 8.80 ± 1.94 | 1.09 ± 0.24 | 33.4 ± 6.5 | 2.47 ± 0.43 | 0.86 ± 0.15 |
| | cpx^free | type III | 2 | 0.06 ± 0.03 | 0.01 ± 0.01 | 0.42 ± 0.21 | 0.04 ± 0.01 | 1.74 ± 0.17 | 5.8 ± 0.3 | 0.16 ± 0.08 | 66.5 ± 1.7 | 1.04 ± 0.05 | 6.37 ± 0.15 | 0.72 ± 0.07 | 16.3 ± 0.3 | 2.27 ± 0.02 | 0.70 ± 0.09 |
| NMM1114 | cpx^free | type I | 17 | 0.07 ± 0.03 | 0.03 ± 0.01 | 0.56 ± 0.25 | 0.07 ± 0.03 | 3.00 ± 0.84 | 10.2 ± 2.4 | 0.22 ± 0.09 | 82.9 ± 20.9 | 1.63 ± 0.37 | 8.03 ± 1.57 | 0.80 ± 0.27 | 25.1 ± 9.5 | 2.30 ± 0.38 | 0.83 ± 0.17 |
| | cpx^opx | | 14 | 0.06 ± 0.02 | 0.02 ± 0.01 | 0.53 ± 0.44 | 0.10 ± 0.05 | 2.14 ± 0.75 | 7.65 ± 2.52 | 0.19 ± 0.04 | 69.5 ± 11.4 | 1.25 ± 0.34 | 6.59 ± 1.93 | 0.62 ± 0.48 | 16.1 ± 10.8 | 2.19 ± 0.98 | 0.73 ± 0.17 |
| NMM1129 | cpx^free | type I | 9 | 0.07 ± 0.04 | 0.03 ± 0.01 | 0.80 ± 0.31 | 0.17 ± 0.06 | 4.79 ± 1.58 | 15.4 ± 3.6 | 0.26 ± 0.13 | 98.5 ± 21.9 | 2.71 ± 0.48 | 14.8 ± 1.1 | 1.96 ± 0.46 | 47.9 ± 12.0 | 4.21 ± 0.55 | 1.39 ± 0.19 |
| | cpx^free | type II | 8 | 0.05 ± 0.01 | 0.02 ± 0.01 | 0.08 ± 0.04 | 0.01 ± 0.01 | 1.51 ± 0.16 | 4.25 ± 0.47 | 0.09 ± 0.02 | 39.2 ± 2.0 | 0.67 ± 0.06 | 3.78 ± 0.26 | 0.89 ± 0.08 | 28.3 ± 1.4 | 1.40 ± 0.19 | 0.564± 0.06 |
| NME1110 | cpx^free | type I | 16 | 0.07 ± 0.03 | 0.02 ± 0.01 | 0.42 ± 0.21 | 0.06 ± 0.04 | 2.91 ± 0.77 | 9.33 ± 2.39 | 0.38 ± 0.32 | 81.0 ± 12.1 | 1.49 ± 0.40 | 7.76 ± 2.13 | 0.68 ± 0.36 | 21.5 ± 9.9 | 2.17 ± 0.51 | 0.79 ± 0.15 |
| | cpx^free | type II | 3 | 0.06 ± 0.01 | 0.02 ± 0.01 | 0.40 ± 0.33 | 0.03 ± 0.01 | 1.72 ± 0.08 | 5.09 ± 0.69 | n.d. | 53.8 ± 4.9 | 0.76 ± 0.06 | 4.57 ± 0.24 | 0.64 ± 0.15 | 18.1 ± 3.4 | 1.53 ± 0.33 | 0.60 ± 0.02 |
| | cpx^free | type III | 3 | 0.07 ± 0.01 | 0.03 ± 0.01 | n.d. | n.d. | 0.62 ± 0.24 | 2.23 ± 0.47 | n.d. | 32.8 ± 2.2 | 0.41 ± 0.06 | 2.68 ± 0.42 | 0.75 ± 0.05 | 20.4 ± 0.5 | 1.16 ± 0.02 | 0.49 ± 0.06 |
| NME1129D | cpx^free | type I | 16 | 0.07 ± 0.04 | 0.03 ± 0.02 | 0.64 ± 0.19 | 0.09 ± 0.06 | 3.59 ± 0.85 | 12.2 ± 2.1 | 0.15 ± 0.08 | 86.9 ± 10.3 | 1.99 ± 0.36 | 10.6 ± 1.9 | 1.14 ± 0.60 | 33.1 ± 15.0 | 3.01 ± 0.57 | 1.04 ± 0.28 |
| | cpx^vermsp | | 6 | 0.11 ± 0.04 | 0.03 ± 0.02 | 0.66 ± 0.19 | 0.13 ± 0.06 | 3.96 ± 0.85 | 13.0 ± 2.1 | 0.20 ± 0.10 | 89.7 ± 10.3 | 2.17 ± 0.36 | 10.6 ± 1.9 | 1.33 ± 0.60 | 34.4 ± 15.0 | 3.13 ± 0.57 | 1.02 ± 0.28 |
| | cpx^opx | | 25 | 0.07 ± 0.03 | 0.03± 0.01 | 0.50 ± 0.23 | 0.06 ± 0.02 | 3.02 ± 0.47 | 10.2 ± 1.2 | n.d. | 86.9 ± 4.5 | 1.67 ± 0.20 | 8.63 ± 1.23 | 0.56 ± 0.34 | 18.3 ± 8.8 | 2.40 ± 0.76 | 0.84 ± 0.13 |

n–number of analyses.
cpx^free–clinopyroxene without orthopyroxene remnants and vermicular spinel.
cpx^opx–clinopyroxene hosting orthopyroxene.
cpx^vermsp–clinopyroxene hosting vermicular spinel.
n.d.–not detected.

In order to constrain the composition of the metasomatic agent, we performed simple calculations based on the average trace element composition of wehrlitic clinopyroxenes (Table 6) and widely accepted alkali silicate melt-clinopyroxene partition coefficients of Hart and Dunn (1993) and Ionov et al. (2002) for the trace elements listed in Table 7. The trace element composition of the inferred melt (Table 7) has a pattern of gradually decreasing abundance towards less incompatible elements with depletion of Th, U, Pb, and Hf (Fig. 10). The trace element concentrations of the inferred equilibrium melt are all above the primitive mantle values, except for Cr and V (McDonough and Sun, 1995). The multi-element pattern of the calculated equilibrium melt shows a good correspondence with both the analyzed (Dobosi et al., 1995) and the

modelled primitive (non-fractionated and non-contaminated) composition of the NGVF host alkali basalt (Zajacz et al., 2007) (Fig. 10; Table 7). A connection is also observed between the calculated equilibrium melt concentrations and the average OIB melt composition of Sun and McDonough (1989) (Fig. 10). These overlaps indicate that the inferred metasomatic agent and the NGVF host basalt are similar in composition and could be related to a comparable mantle source and melting event resulting in an OIB-like melt character.

### 9.2.3. Evolution of the composition of the metasomatic agent during metasomatism

The pristine (un-reacted) metasomatic mafic melt composition must

**CLINOPYROXENE**

| Gd | Tb | Ti | Dy | Ho | Y | Er | Tm | Yb | Lu | Sc | V | Cr | Co | Ni | ΣREE | $(La/Lu)_N$ | $(Nd/Yb)_N$ |
|---|---|---|---|---|---|---|---|---|---|---|---|---|---|---|---|---|---|
| 1.67 ± 0.25 | 0.24 ± 0.05 | 2682 ± 863 | 1.66 ± 0.34 | 0.34 ± 0.06 | 8.46 ± 0.80 | 0.875 ± 0.199 | 0.14 ± 0.03 | 0.88 ± 0.19 | 0.13 ± 0.03 | 27.2 ± 9.6 | 241 ± 20 | 7849 ± 1303 | 25.0 ± 2.9 | 338 ± 26 | 22.74 | 1.55 | 2.18 |
| 1.51 ± 0.24 | 0.24 ± 0.04 | 1892 ± 207 | 1.67 ± 0.48 | 0.34 ± 0.06 | 9.05 ± 1.07 | 1.11 ± 0.22 | 0.12 ± 0.01 | 0.95 ± 0.23 | 0.13 ± 0.01 | 42.5 ± 2.8 | 258 ± 21 | 8394 ± 1689 | 24.1 ± 2.5 | 359 ± 14 | 18.88 | 1.11 | 1.53 |
| 1.62 ± 0.30 | 0.26 ± 0.05 | 2560 ± 698 | 1.60 ± 0.21 | 0.34 ± 0.08 | 8.76 ± 1.28 | 0.97 ± 0.19 | 0.13 ± 0.03 | 0.84 ± 0.22 | 0.13 ± 0.04 | 30.3 ± 12.1 | 232 ± 18 | 7281 ± 641 | 24.7 ± 2.3 | 344 ± 24 | 21.87 | 1.51 | 2.14 |
| 2.41 ± 0.27 | 0.36 ± 0.08 | 1713 ± 646 | 2.37 ± 0.42 | 0.49 ± 0.10 | 11.9 ± 1.7 | 1.34 ± 0.19 | 0.19 ± 0.05 | 1.29 ± 0.22 | 0.17 ± 0.03 | 32.5 ± 3.7 | 224 ± 20 | 8614 ± 2769 | 22.0 ± 2.3 | 291 ± 57 | 46.64 | 3.10 | 3.10 |
| 2.56 ± 0.14 | 0.39 ± 0.04 | 1678 ± 554 | 2.56 ± 0.14 | 0.50 ± 0.04 | 12.6 ± 0.3 | 1.38 ± 0.05 | 0.19 ± 0.01 | 1.31 ± 0.14 | 0.19 ± 0.02 | 29.8 ± 1.6 | 221 ± 25 | 9015 ± 1871 | 24.6 ± 5.8 | 340 ± 95 | 46.17 | 2.62 | 2.92 |
| 2.54 ± 0.40 | 0.36 ± 0.06 | 2123 ± 688 | 2.27 ± 0.28 | 0.44 ± 0.07 | 11.1 ± 1.2 | 1.23 ± 0.13 | 0.17 ± 0.02 | 1.17 ± 0.11 | 0.16 ± 0.02 | 30.5 ± 2.5 | 225 ± 35 | 8078 ± 2526 | 21.0 ± 2.0 | 252 ± 33 | 47.48 | 3.03 | 3.58 |
| 2.49 ± 0.32 | 0.40 ± 0.06 | 2942 ± 1085 | 2.75 ± 0.43 | 0.55 ± 0.09 | 14.0 ± 2.3 | 1.58 ± 0.30 | 0.22 ± 0.04 | 1.49 ± 0.25 | 0.21 ± 0.04 | 33.1 ± 3.4 | 253 ± 61 | 6159 ± 1338 | 20.8 ± 1.5 | 273 ± 26 | 37.54 | 1.65 | 2.11 |
| 2.58 ± 0.43 | 0.39 ± 0.08 | 3235 ± 1095 | 2.55 ± 0.55 | 0.49 ± 0.09 | 12.9 ± 2.2 | 1.41 ± 0.20 | 0.19 ± 0.04 | 1.26 ± 0.17 | 0.19 ± 0.02 | 33.5 ± 2.6 | 249 ± 40 | 7041 ± 1375 | 24.6 ± 2.0 | 323 ± 28 | 36.12 | 1.67 | 2.45 |
| 1.95 ± 0.21 | 0.35 ± 0.04 | 1428 ± 399 | 2.53 ± 0.30 | 0.56 ± 0.06 | 13.9 ± 1.4 | 1.67 ± 0.24 | 0.24 ± 0.02 | 1.62 ± 0.13 | 0.23 ± 0.03 | 29.9 ± 3.1 | 183 ± 18 | 4183 ± 310 | 18.9 ± 1.6 | 268 ± 31 | 31.68 | 1.71 | 1.24 |
| 2.83 ± 0.61 | 0.42 ± 0.05 | 6513 ± 1394 | 2.85 ± 0.54 | 0.51 ± 0.07 | 13.0 ± 1.6 | 1.40 ± 0.19 | 0.17 ± 0.07 | 1.20 ± 0.22 | 0.16 ± 0.02 | 44.2 ± 3.0 | 276 ± 12 | 6429 ± 1020 | 23.9 ± 1.0 | 241 ± 24 | 37.30 | 2.09 | 2.77 |
| 3.20 ± 0.46 | 0.46 ± 0.07 | 7588 ± 1008 | 2.93 ± 0.28 | 0.55 ± 0.08 | 13.0 ± 1.2 | 1.28 ± 0.18 | 0.19 ± 0.07 | 1.17 ± 0.39 | 0.17 ± 0.06 | 39.9 ± 2.4 | 291 ± 16 | 5864 ± 933 | 23.9 ± 1.3 | 229 ± 22 | 41.18 | 2.13 | 3.16 |
| 1.93 ± 0.37 | 0.28 ± 0.06 | 2641 ± 660 | 1.83 ± 0.31 | 0.37 ± 0.08 | 9.0 ± 1.3 | 1.00 ± 0.19 | 0.14 ± 0.02 | 0.94 ± 0.19 | 0.14 ± 0.03 | 30.4 ± 6.6 | 245 ± 31 | 7548 ± 730 | 21.8 ± 0.8 | 278 ± 59 | 29.92 | 2.10 | 2.81 |
| 1.81 ± 0.28 | 0.33 ± 0.05 | 1895 ± 248 | 2.23 ± 0.33 | 0.48 ± 0.06 | 11.8 ± 1.4 | 1.31 ± 0.23 | 0.19 ± 0.03 | 1.29 ± 0.17 | 0.18 ± 0.03 | 34.6 ± 1.5 | 238 ± 19 | 5624 ± 1127 | 21.2 ± 0.9 | 340 ± 19 | 29.23 | 2.70 | 1.73 |
| 2.70 ± 0.49 | 0.49 ± 0.10 | 3972 ± 1733 | 3.49 ± 0.71 | 0.76 ± 0.16 | 19.3 ± 4.2 | 2.18 ± 0.50 | 0.32 ± 0.06 | 2.00 ± 0.42 | 0.28 ± 0.06 | 42.2 ± 4.7 | 369 ± 124 | 6843 ± 1931 | 21.5 ± 0.9 | 324 ± 19 | 31.49 | 4.15 | 1.07 |
| 1.43 ± 0.23 | 0.26 ± 0.05 | 2065 ± 286 | 1.81 ± 0.28 | 0.38 ± 0.08 | 10.1 ± 1.2 | 1.12 ± 0.17 | 0.16 ± 0.06 | 0.99 ± 0.38 | 0.16 ± 0.06 | 34.9 ± 1.6 | 242 ± 8 | 8103 ± 772 | 21.5 ± 2.4 | 325 ± 25 | 16.26 | 0.64 | 1.09 |
| 1.38 ± 0.31 | 0.21 ± 0.04 | 2339 ± 466 | 1.39 ± 0.26 | 0.30 ± 0.04 | 7.76 ± 0.53 | 0.80 ± 0.17 | 0.11 ± 0.05 | 0.65 ± 0.28 | 0.09 ± 0.05 | 31.1 ± 1.3 | 215 ± 9 | 8067 ± 438 | 25.1 ± 4.8 | 318 ± 40 | 20.94 | 2.18 | 2.77 |
| 2.28 ± 0.50 | 0.40 ± 0.06 | 2303 ± 1377 | 2.78 ± 0.33 | 0.59 ± 0.08 | 14.9 ± 1.9 | 1.65 ± 0.15 | 0.24 ± 0.02 | 1.62 ± 0.16 | 0.23 ± 0.03 | 35.6 ± 3.3 | 236 ± 35 | 5895 ± 528 | 21.6 ± 0.7 | 313 ± 15 | 32.58 | 1.40 | 1.46 |
| 2.61 ± 0.54 | 0.46 ± 0.10 | 4027 ± 751 | 3.17 ± 0.64 | 0.66 ± 0.12 | 17.6 ± 3.0 | 1.90 ± 0.32 | 0.28 ± 0.03 | 1.71 ± 0.30 | 0.27 ± 0.06 | 37.7 ± 1.4 | 287 ± 22 | 7661 ± 547 | 22.9 ± 0.9 | 285 ± 12 | 33.94 | 0.89 | 1.54 |
| 2.74 ± 0.52 | 0.43 ± 0.09 | 3894 ± 1340 | 2.75 ± 0.55 | 0.55 ± 0.11 | 14.1 ± 2.4 | 1.51 ± 0.30 | 0.21 ± 0.05 | 1.43 ± 0.32 | 0.18 ± 0.05 | 74.1 ± 39.5 | 265 ± 49 | 5900 ± 1690 | 22.0 ± 1.7 | 308 ± 29 | 37.74 | 2.07 | 2.15 |
| 2.45 ± 0.13 | 0.45 ± 0.04 | 5392 ± 501 | 2.65 ± 0.20 | 0.59 ± 0.15 | 14.8 ± 0.1 | 1.64 ± 0.21 | 0.21 ± 0.02 | 1.39 ± 0.04 | 0.17 ± 0.01 | 37.2 ± 0.2 | 320 ± 26 | 9279 ± 179 | 21.9 ± 0.6 | 290 ± 1 | 27.45 | 1.05 | 1.61 |
| 2.45 ± 0.47 | 0.38 ± 0.05 | 3658 ± 1620 | 2.47 ± 0.28 | 0.46 ± 0.10 | 12.2 ± 1.8 | 1.28 ± 0.29 | 0.20 ± 0.05 | 1.29 ± 0.32 | 0.18 ± 0.04 | 34.0 ± 2.2 | 254 ± 43 | 5964 ± 1997 | 24.5 ± 3.2 | 270 ± 51 | 46.90 | 1.75 | 2.19 |
| 2.10 ± 0.63 | 0.33 ± 0.09 | 4219 ± 1852 | 2.04 ± 0.51 | 0.43 ± 0.12 | 10.1 ± 2.6 | 1.03 ± 0.27 | 0.16 ± 0.04 | 1.01 ± 0.29 | 0.14 ± 0.03 | 31.1 ± 2.3 | 255 ± 40 | 5241 ± 1928 | 26.5 ± 1.6 | 262 ± 43 | 27.79 | 1.60 | 2.30 |
| 4.25 ± 0.48 | 0.61 ± 0.09 | 8283 ± 6011 | 4.15 ± 0.44 | 0.80 ± 0.11 | 19.1 ± 2.4 | 1.94 ± 0.20 | 0.27 ± 0.05 | 1.78 ± 0.32 | 0.23 ± 0.05 | 34.1 ± 5.8 | 240 ± 73 | 4760 ± 2208 | 27.2 ± 7.6 | 329 ± 72 | 76.43 | 2.21 | 2.94 |
| 1.94 ± 0.22 | 0.344 ± 0.02 | 1944 ± 137 | 2.64 ± 0.14 | 0.54 ± 0.03 | 13.8 ± 0.7 | 1.54 ± 0.06 | 0.22 ± 0.02 | 1.54 ± 0.05 | 0.20 ± 0.02 | 35.7 ± 0.4 | 206 ± 9 | 4273 ± 307 | 21.4 ± 0.7 | 324 ± 16 | 21.13 | 0.78 | 0.87 |
| 2.36 ± 0.55 | 0.36 ± 0.08 | 4406 ± 1505 | 2.38 ± 0.46 | 0.45 ± 0.07 | 11.8 ± 1.7 | 1.28 ± 0.18 | 0.18 ± 0.03 | 1.12 ± 0.16 | 0.16 ± 0.03 | 36.4 ± 3.0 | 258 ± 28 | 6809 ± 1306 | 24.2 ± 2.2 | 317 ± 44 | 32.73 | 1.50 | 1.02 |
| 2.22 ± 0.07 | 0.33 ± 0.02 | 2756 ± 439 | 2.60 ± 0.35 | 0.48 ± 0.04 | 13.5 ± 0.7 | 1.36 ± 0.26 | 0.19 ± 0.01 | 1.30 ± 0.08 | 0.18 ± 0.05 | 39.1 ± 0.7 | 256 ± 29 | 6617 ± 1238 | 22.5 ± 1.2 | 321 ± 16 | 22.94 | 1.04 | 1.24 |
| 1.65 ± 0.32 | 0.33 ± 0.03 | 2005 ± 36 | 2.67 ± 0.16 | 0.58 ± 0.02 | 14.3 ± 0.4 | 1.70 ± 0.06 | 0.24 ± 0.03 | 1.42 ± 0.08 | 0.23 ± 0.07 | 35.9 ± 1.0 | 235 ± 4 | 4977 ± 28 | 21.6 ± 1.3 | 359 ± 8 | 16.40 | 0.31 | 0.67 |
| 3.20 ± 1.06 | 0.43 ± 0.12 | 6820 ± 2814 | 2.68 ± 0.64 | 0.53 ± 0.15 | 13.6 ± 2.6 | 1.45 ± 0.18 | 0.19 ± 0.03 | 1.18 ± 0.32 | 0.18 ± 0.07 | 29.9 ± 1.1 | 295 ± 66 | 4423 ± 2625 | 23.6 ± 2.0 | 241 ± 66 | 42.30 | 2.08 | 3.19 |
| 3.07 ± 1.06 | 0.44 ± 0.12 | 6933 ± 2814 | 2.95 ± 0.64 | 0.53 ± 0.15 | 13.0 ± 2.6 | 1.33 ± 0.18 | 0.17 ± 0.03 | 1.26 ± 0.36 | 0.17 ± 0.04 | 29.1 ± 1.1 | 298 ± 66 | 4092 ± 2625 | 25.7 ± 2.0 | 191 ± 66 | 43.81 | 1.69 | 2.96 |
| 2.33 ± 0.54 | 0.34 ± 0.07 | 3675 ± 1532 | 2.08 ± 0.43 | 0.41 ± 0.11 | 10.6 ± 1.3 | 1.12 ± 0.19 | 0.16 ± 0.03 | 1.00 ± 0.19 | 0.15 ± 0.03 | 28.3 ± 2.8 | 233 ± 21 | 6126 ± 1088 | 25.1 ± 1.8 | 271 ± 52 | 34.30 | 2.14 | 3.04 |

have evolved as a result of geochemical interaction with the lherzolitic mantle. The main driver of the compositional change could be the dissolution of orthopyroxene to produce a Si-rich melt (e.g., Kelemen, 1990), which subsequently mixes with the pristine metasomatic melt. The resulting modified melt with intermediate $SiO_2$ content is consistent with the compositions of silicate melt inclusions hosted by wehrlitic olivines and clinopyroxenes (51.1–56.4 wt.% with an average of 54.0 wt.%; Patkó et al., 2018). Chemical evolution of the metasomatizing agent continues until the mixture of the pristine and the modified melts quasi-equilibrates with the wall rock peridotite assemblage and becomes orthopyroxene-saturated (Shaw et al., 2018). This inferred evolution in the composition of the metasomatic melt is reflected in the composition of the newly-formed clinopyroxenes that retain orthopyroxene remnants in their cores (Fig. 2g). Clinopyroxene grains with such textures have the lowest $TiO_2$, $Al_2O_3$ and CaO, but the highest $SiO_2$ and MgO content among all clinopyroxenes in wehrlites (Figs. 4b and 11; Table 3). This change in geochemistry occurs because the dissolving orthopyroxenes locally have a large effect on the pristine melt composition. The result is

the enrichment ($SiO_2$, MgO) or depletion of elements ($TiO_2$, $Al_2O_3$, CaO) in the clinopyroxenes, in agreement with elemental partitioning preferences between orthopyroxene and clinopyroxene. However, trace element patterns among clinopyroxenes in the various textural occurrences show no differences (Supplementary Fig. 5), probably because of the slow diffusion rate of the trivalent REEs compared to the divalent major cations (e.g., Ca, Fe, Mn) in orthopyroxenes (Cherniak and Liang, 2007). Accordingly, the orthopyroxene transformation into clinopyroxene probably happened at a rate that was faster than the trace element equilibration time. Alternatively, the nearly two orders of magnitude lower LREE concentration in lherzolitic orthopyroxenes, compared to those in coexisting clinopyroxenes (Liptai et al., 2017), was too low to significantly dilute the composition of the metasomatic agent. It is also possible that the higher trace element content of the pristine melt can compensate for the dilution effect.

During the wehrlitization process in the NGVF mantle, incongruent orthopyroxene breakdown had not gone to completion (Table 4; Fig. 2b, g) because the metasomatic agent continued to migrate before becoming
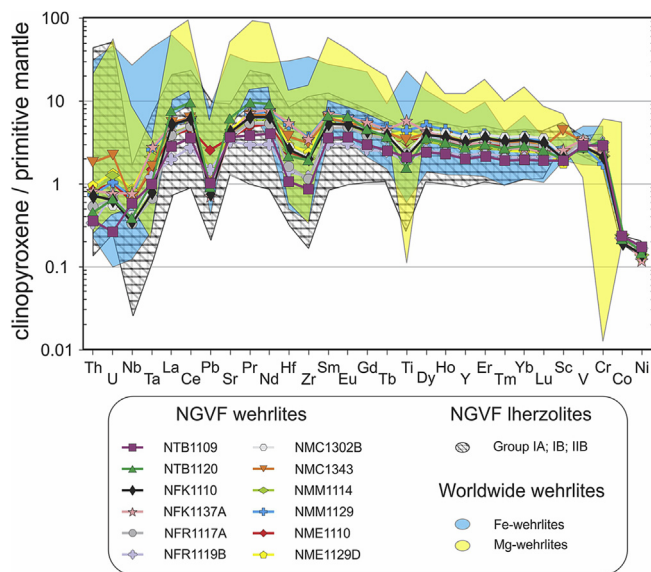
**Fig. 6.** Primitive mantle (McDonough and Sun, 1995) normalized multi-element diagram for clinopyroxenes. The NGVF lherzolites are from Liptai et al. (2017). The reference Fe-wehrlites are based on: Xu et al. (1996); Rivalenti et al. (2004); Shaw et al. (2005); Raffone et al. (2009); Xiao et al. (2010). The reference Mg-wehrlites are based on: Hauri et al. (1993); Xu et al. (1996); Coltorti et al. (1999); Neumann et al. (2002); Raffone et al. (2009); Scott et al. (2014).

orthopyroxene saturated. Another possibility is that the metasomatic melt was no longer reactive because it became orthopyroxene saturated. Temperature influences the rate of orthopyroxene dissolution, and cooling of the metasomatic agent can lead to slower consumption of orthopyroxenes (Tursack and Liang, 2012). According to Saper and Liang (2014), the slower the melt-rock interaction and the higher the melt/rock ratio, the more intensive the orthopyroxene dissolution. Other experimental results of Mitchell and Grove (2016) argue that at least 20% melt fraction is needed for wehrlite formation. Based on thermodynamic modelling of Shaw et al. (2018), the amount of melt required to produce wehrlite depends on the temperature (melt/rock ratio decreases from 0.67 at 1000 °C to 0.11 at 1200–1300 °C). Accordingly, for our plate model calculation (discussed below in section 9.5) the melt/rock ratio for the NGVF wehrlites was assumed to be ~0.3, which indicates that the preservation of orthopyroxenes is likely not because of the low melt/rock ratio during metasomatism, but rather was due to orthopyroxene over-saturation of the melt.

It is known that the volatile content influences the orthopyroxene dissolution rate, i.e., the dissolution rate under hydrous conditions (using synthetic basanite glass with 4 wt.% $H_2O$ as a starting material) is ~ 3-times faster due to enhanced diffusion (Shaw, 1999). Fourier-transform infrared (FTIR) spectroscopic analysis of nominally anhydrous minerals in the NGVF wehrlites show higher bulk structural hydroxyl content (~63 ppm) compared to the NGVF lherzolites (~17 ppm) (Patkó et al., 2019). This suggests structural hydroxyl enrichment in wehrlite clinopyroxenes compared to lherzolites due to interaction with the metasomatic melt. In contrast, $CO_2$ has the opposite effect on the rate of orthopyroxene dissolution, compared to $H_2O$ (Shaw et al., 1999). Carbon-dioxide is present in the bubbles in silicate melt inclusions (Patkó et al., 2018) and in fluid inclusions (Szabó and Bodnar, 1996, 1998) in the metasomatized Nógrád-Gömör peridotite xenoliths. The calculated $CO_2$ contents (1.27–1.94 wt.%) are significantly higher than the measured $H_2O$ concentrations (0.14–0.67 wt.%) in silicate melt inclusions that probably trapped the metasomatic agent (Szabó et al., 1996). Consequently, $CO_2$ might have played a role in orthopyroxene preservation.
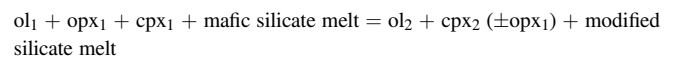
The presence of vermicular spinels (Fig. 2e) could also be associated with changes in the composition of the metasomatic agent. Vermicular spinels were also observed to become Cr-rich as a result of complex mixing of pristine and evolved melts in the chromitite zone of an ultramafic complex (Arai and Yurimoto, 1994), and in experimental runs (Ballhaus, 1998). The vermicular spinels, also reported in Fe-wehrlites (Ionov et al., 2005; Raffone et al., 2009) and in melt-rock reaction experiments (Van Den Bleeken et al., 2010), occur in four of the studied wehrlites (NTB1109, NTB1120, NFK1137A, NME1129D). The vermicular spinels are Cr-enriched and Al-depleted compared to interstitial spinels in the same xenoliths (Table 5; Fig. 4c). Chromium, being highly compatible during dissolution, remains fixed providing relative enrichment, whereas Al, which is incompatible, is partitioned into the metasomatic melt, leaving behind a depleted signature (e.g., Dick et al., 1984). Therefore, spinel nuggets probably represent breakdown remnants of former interstitial spinels, after metasomatism-induced dissolution.

According to Suhr et al. (2008), orthopyroxene dissolution can lead to Cr saturation in the silicate melt and subsequent spinel precipitation. During this process, the metasomatic melt could become oversaturated in Si and dissolve olivine locally. The remnants that remain after olivine dissolves are clinopyroxene-spinel assemblages with a clinopyroxene–spinel ratio, which agrees with our estimations (Fig. 2f). Such an origin via dissolution is further supported by the observation that the vermicular spinels are present exclusively in newly-formed clinopyroxenes (Fig. 2e). However, compositional recombination of the vermicular spinel and their host clinopyroxene resulted in extremely high $Cr_2O_3$ (4.63–7.45 wt.%) and $Al_2O_3$ (11.8–21.0 wt.%) concentrations, which is inconsistent with these elements having been incorporated in former olivines or being transported in metasomatic melts. Therefore, olivine dissolution is unlikely to have caused the vermicular spinel formation in the NGVF mantle.

### 9.3. The extent of metasomatism

Based on petrographic observations and geochemical features, wehrlites are considered to be the result of mantle metasomatism according to the following:

$ol_1 + opx_1 + cpx_1$ + mafic silicate melt = $ol_2 + cpx_2 (\pm opx_1)$ + modified silicate melt

where $ol_1$, $opx_1$ and $cpx_1$ denote the minerals of the precursor lherzolite, whereas the $ol_2$ and $cpx_2$ represent the geochemically modified or newly formed minerals of the wehrlites. The orthopyroxene remnants appear as $opx_1$ on the right side of the equation. The mafic silicate melt is the pristine metasomatic agent, which is modified by orthopyroxene dissolution (and spinel dissolution to a lesser extent) leading to a more evolved modified silicate melt (discussed above in section 9.2.3). The process associated with the increase in clinopyroxene proportion at the expense of orthopyroxene is referred to as stealth mantle metasomatism (O'Reilly and Griffin, 2013). Comparing the Mg# of the wehrlitic silicates with each other and with the Cr# of spinels, positive correlations can be observed (Fig. 12), in which the lower Mg# and Cr# values (vermicular spinels were excluded) correspond to higher degrees of metasomatism (Tables 2–4). Accordingly, xenoliths NTB1109, NFR1119B, NMC1302B and NMC1343 are the least (olivine Mg# > 0.87; clinopyroxene Mg# > 0.88 and spinel Cr# > 0.19) metasomatized, whereas xenoliths NTB1120, NFK1110 and NMM1129 are metasomatized to the greatest extent (olivine Mg# < 0.86; clinopyroxene Mg# < 0.86 and spinel Cr# < 0.20) during the wehrlitization (Fig. 12). Indeed, xenoliths NTB1109, NFR1119B, NMC1302B and NMC1343 have low clinopyroxene contents (<22 vol.%; Table 1), and the prior two contain no clinopyroxene- and olivine-rich areas, in contrast to the other wehrlite xenoliths (Supplementary Fig. 1a and b). Furthermore, xenoliths NTB1109, NFR1119B and NMC1343 have the lowest basaltic major element (Fe, Mn, Ti) and LREE concentrations, both in rock-forming mineral (Figs. 3 and 7) and bulk
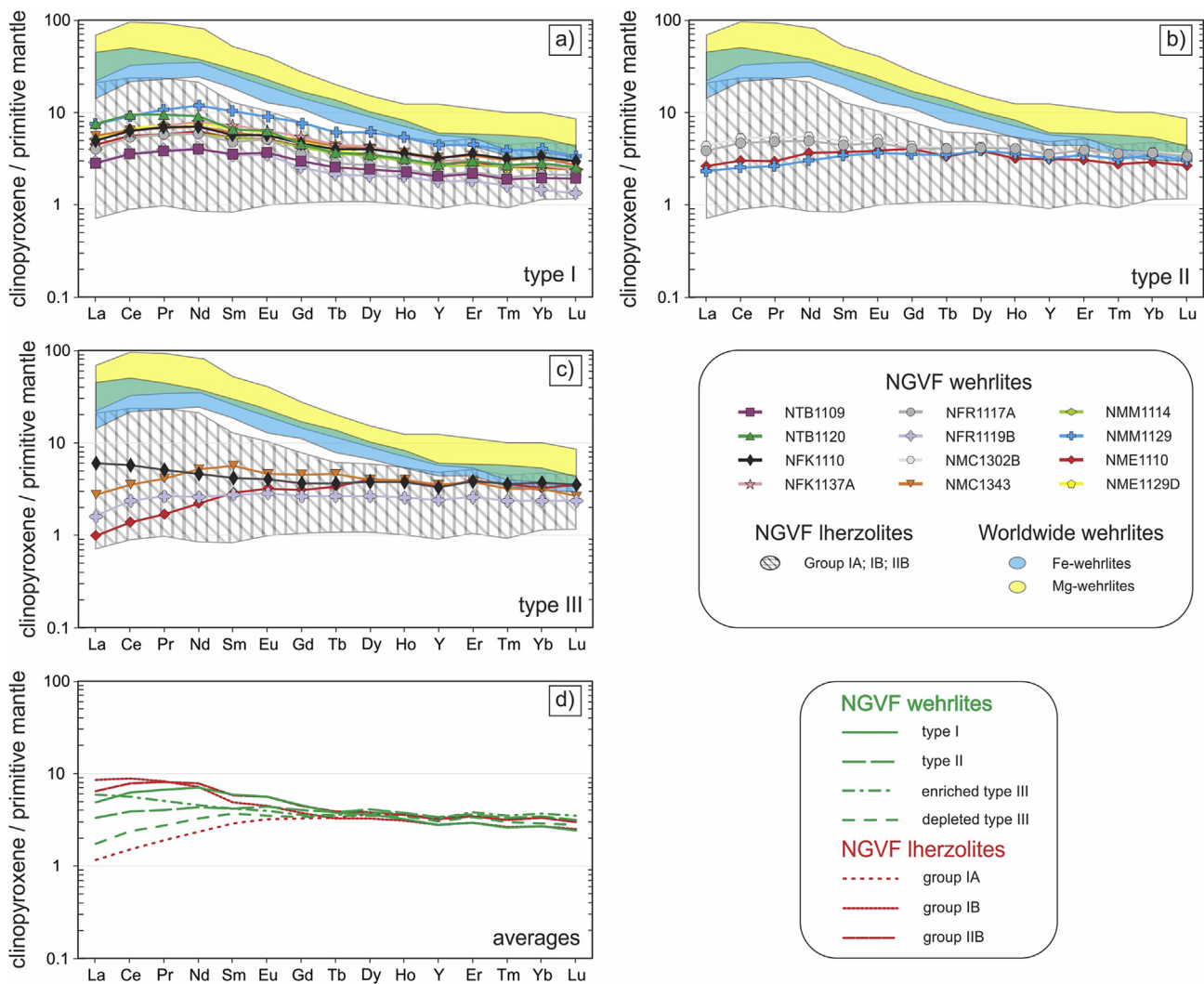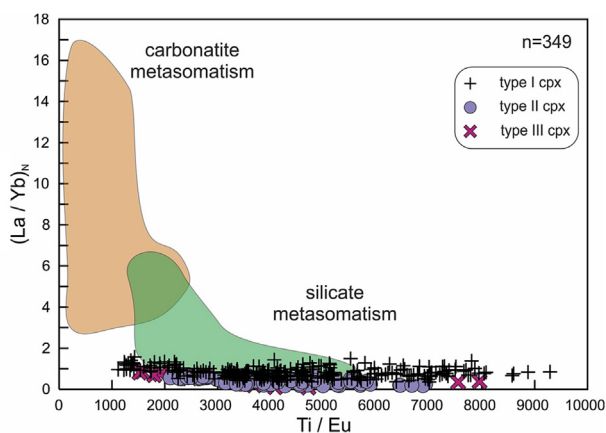
**Fig. 7.** Primitive mantle (McDonough and Sun, 1995) normalized REY patterns of **(a)** type I, **(b)** type II, and **(c)** type III clinopyroxenes of wehrlite xenoliths. **(d)** The average REY distributions for different clinopyroxene types from wehrlites along with those from distinct lherzolites based on Liptai et al. (2017). The reference Fe-wehrlites are based on: Xu et al. (1996); Rivalenti et al. (2004); Shaw et al. (2005); Raffone et al. (2009); Xiao et al. (2010). The reference Mg-wehrlites are based on: Hauri et al. (1993); Xu et al. (1996); Coltorti et al. (1999); Neumann et al. (2002); Raffone et al. (2009); Scott et al. (2014).



**Fig. 8.** $(La/Yb)_N$ vs. Ti/Eu of the different clinopyroxene groups of wehrlite xenoliths. Areas of silicate and carbonate metasomatism are from Coltorti et al. (1999).

rock compositions (Supplementary Figs. 3 and 4). In contrast, xenoliths NTB1120, NFK1110 and NMM1129 show high basaltic element content, both in rock-forming minerals and in the bulk rocks (Fig. 3; Supplementary Fig. 3), as well as high concentrations for LREE (Fig. 7) and HFSE (Fig. 6). The positive correlation of Mg# among olivine and pyroxenes (Fig. 12a and b) indicates a single event causing differential enrichment, which affected the entire mineral assemblage.

It is also important to note that the differences in the degree of metasomatism were found not only between but within xenoliths as well. For example, clinopyroxene compositions in xenoliths NFK1110, NME1110 and NME1129D vary over nearly the whole $Al_2O_3$ vs. $TiO_2$ range (Fig. 4b) that is defined by all 12 wehrlites studied (Fig. 3b). This variability suggests that some areas of single xenoliths are affected more than other areas in the same xenolith. Similarly, olivines and spinels also show intra-xenolith heterogeneities (Fig. 4a, c). The strongest intra-xenolith heterogeneities are mostly linked to weakly or moderately metasomatized xenoliths. One possible reason to explain why the wide ranges in geochemistry (Fig. 4) are not detected in all xenoliths is related to the areal (or volumetric) extent of the heterogeneities. In some xenoliths (NFK1110, NME1110, NME1129D), the area in which heterogeneities are observed is smaller (μm–mm range) than the size of the xenolith (3–5 cm), whereas in other xenoliths (NMC1343, NM1114) the
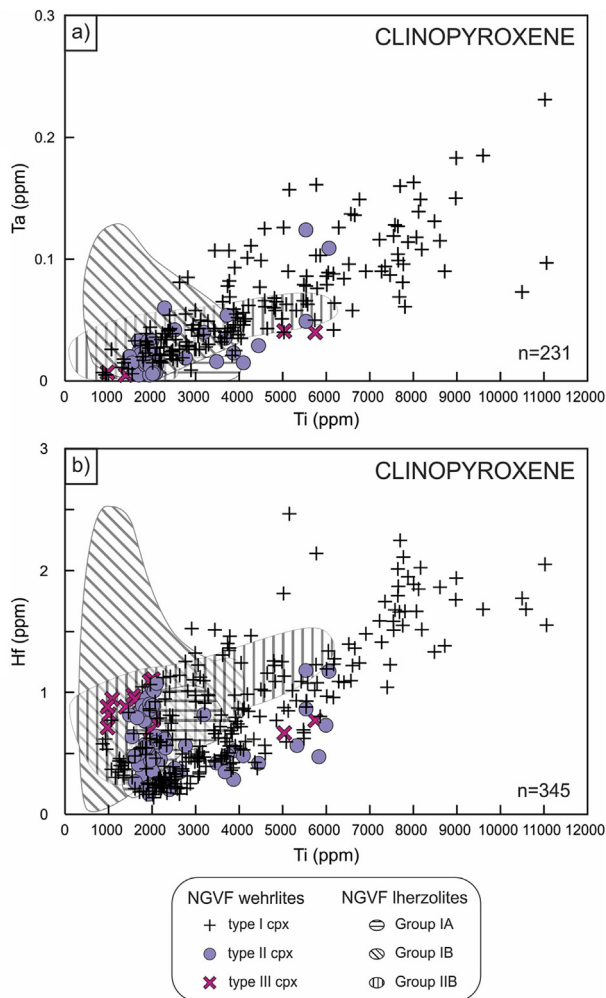
**Fig. 9.** Relationships between **(a)** Ti vs. Ta and **(b)** Ti vs. Hf for the different clinopyroxene groups in wehrlite xenoliths. Reference lherzolite data are from Liptai et al. (2017).

**Table 7**

Results of the equilibrium melt composition calculation. The input solid phase compositions are the average values of the trace element measurements. The partition coefficients used here for Th, U, Nb, Ta, La, Ce, Pb, Sr, Pr, Nd, Hf, Zr, Sm, Eu, Gd, Tb, Ti, Dy, Ho, Er, Tm, Tb, Lu are from Ionov et al. (2002), and for Y, Sc, V, Cr are from Hart and Dunn (1993). The estimated primitive (non-fractionated, non-contaminated) host basalt composition is obtained from cumulates (Zajacz et al., 2007). The whole rock composition of the host basalt is based on X-ray fluorescence spectrometry (Dobosi et al., 1995).

| Element | Calculated melt agent composition (ppm) | Estimated host basalt composition (ppm) (Zajacz et al., 2007) | Whole rock compositions of the host basalt (ppm) (Dobosi et al., 1995) |
|---|---|---|---|
| Th | 5.3 | 3.0 | 7.6 |
| U | 1.9 | 1.3 | – |
| Nb | 49.1 | 36.0 | 86.2 |
| Ta | 2.8 | 2.3 | – |
| La | 54.3 | 30.0 | 50.4 |
| Ce | 109 | 58.0 | 92.2 |
| Pb | 2.1 | 3.0 | – |
| Sr | 620 | 592 | 846 |
| Pr | 10.9 | – | – |
| Nd | 41.4 | 30.0 | 41.5 |
| Hf | 3.8 | 3.4 | 4.4 |
| Zr | 167 | 174 | 229 |
| Sm | 7.5 | 5.9 | 7.1 |
| Eu | 2.3 | 2.0 | 2.0 |
| Gd | 5.8 | – | – |
| Tb | 0.9 | 0.7 | 0.7 |
| Ti | 11630 | 11750 | 11995 |
| Dy | 5.5 | – | – |
| Ho | 1.1 | – | – |
| Y | 26.5 | 20.0 | 28.7 |
| Er | 3.1 | – | – |
| Tm | 0.4 | – | – |
| Yb | 2.9 | 2.0 | 2.5 |
| Lu | 0.4 | 0.2 | 0.3 |
| Sc | 25.7 | 27.0 | 19.8 |
| V | 81.5 | 164 | 184 |
| Cr | 1713 | 381 | 132 |

areal extent of heterogeneities is probably larger (>5 cm) than the dimension of the xenolith. This likely reflects the local characteristics of the melt (e.g. amount, reactivity) or physical features (e.g. better migration pathways). The degree or extent of metasomatism of the various xenoliths show no spatial correlation (Supplementary Fig. 6), suggesting that metasomatized mantle is present under the entirety of the central NGVF.

### 9.4. Temperature-pressure conditions of wehrlite formation

In order to calculate an equilibrium temperature that is meaningful, coexisting minerals in the sample should show evidence of textural and chemical equilibrium. However, the studied wehrlites are characterized by a lack of equigranular texture, increase in the proportion of clinopyroxene at the expense of orthopyroxene (Fig. 2g), together with the compositional heterogeneity of the rock-forming minerals (Fig. 3; Tables 2–5), not only among xenoliths, but even within grains (e.g. in xenoliths NFK1110, NME1110, NME1129D) (Fig. 4). All of these features suggest that rock-forming minerals did not achieve chemical equilibrium with each other, and thus equilibrium temperature estimations based on these phases are unreliable. However, rounded orthopyroxene relicts enclosed by olivines are present in some wehrlite xenoliths (NFR1117A, NFR1119B, NMC1302B, NMC1343, NMM1114; Table 4) (Fig. 2b). These

orthopyroxene remnants in olivines have compositional similarity on an $Al_2O_3$–CaO variation plot with Group IA, IB and IIB NGVF lherzolites as classified by Liptai et al. (2017) (Fig. 5a). Also, the orthopyroxenes in olivine are different from those hosted by newly formed clinopyroxenes, which have systematically elevated CaO contents (Fig. 5a). However, other elements (e.g., FeO, MnO) in orthopyroxenes show no systematic differences as a function of their textural occurrence (Fig. 5b). These observations indicate that orthopyroxene inclusions in olivine were not affected by Ca enrichment, probably due to the mechanical and chemical isolation provided by their host mineral. Therefore, in some cases, olivine hosts might have hindered direct contact between the metasomatic agent and the orthopyroxene by acting as a physical barrier. This interpretation is further supported by the slower diffusion rate for Ca compared to other cations, such as Fe and Mn, in the olivine structure (Coogan et al., 2005 and references therein). Both alternatives assume that such orthopyroxenes (Fig. 2b) already existed before the wehrlitization process started.

It is worth investigating whether the olivine could have formed directly from orthopyroxene (e.g., Shaw et al., 2018). Newly formed clinopyroxene at the edge of orthopyroxene inclusions hosted by olivines (Fig. 2c) indicates that clinopyroxene is more likely to form than olivine at the expense of orthopyroxene during metasomatism beneath the NGVF. Consequently, the modified Ca-in-opx thermometer ($T_{Ca-in-opx}$, Nimis and Grütter, 2010) was applied to orthopyroxene inclusions in olivine to estimate the pre-wehrlitization thermal conditions of the later transformed mantle. The calculated equilibration temperatures are of 985–1055 °C ($T_{Ca-in-opx}$) (Table 1), which is similar to those of the central NGVF lherzolite xenoliths which show a range of 940–1040 °C ($T_{Ca-in-opx}$) (Liptai et al., 2017 and on data of Szabó and Taylor, 1994; Konečný et al., 1999). This difference is within the error of the geothermometers (±36
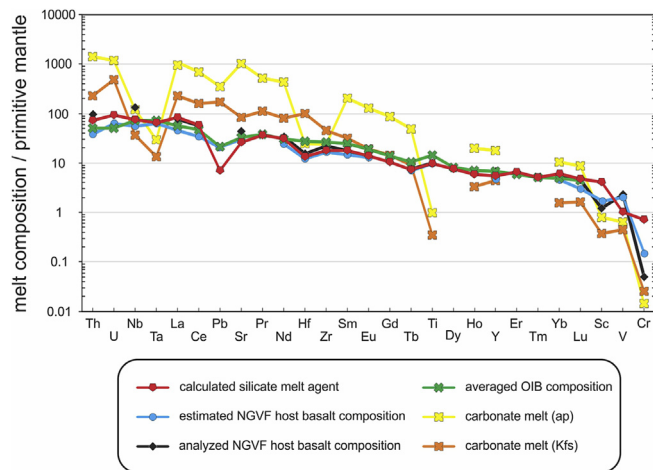
**Fig. 10.** Estimated trace element composition of the metasomatic agent using the averaged trace element composition of wehrlitic clinopyroxenes and silicate melt-clinopyroxene partition coefficients of Ionov et al. (2002) for Th, U, Nb, Ta, La, Ce, Pb, Sr, Pr, Nd, Hf, Zr, Sm, Eu, Gd, Tb, Ti, Dy, Ho, Er, Tm, Yb and Lu; and Hart and Dunn (1993) for Y, Sc, V and Cr. The obtained primitive mantle (McDonough and Sun, 1995) normalized trace element distribution is compared to the trace element composition of the estimated local non-fractionated, non-contaminated host alkali basalt based on cumulates (Zajacz et al., 2007); the average trace element composition of the analyzed host alkali basalts (Dobosi et al., 1995); the average trace element composition of the ocean island basalts (Sun and McDonough, 1989) and the trace element composition of carbonate melt based on melt inclusions hosted by apatites (carbonatite ap; Guzmics et al., 2008) and potassium feldspars (carbonatite Kfs; Guzmics et al., 2008).

°C for $T_{Ca-in-opx}$) and, therefore, cannot distinguish between equilibrium in a hot mantle volume or origination at greater depths. Note, however, that equilibration temperatures of lherzolite xenoliths are usually higher in the central NGVF compared to those from the northern and southern localities (Liptai et al., 2017), which is probably due to the extensive thermal effect of the wehrlitization process. According to Liptai et al. (2019), this extra heat may have led to post-kinematic annealing that is observed in the microstructures of the xenoliths.

The wehrlites are all derived from the spinel facies zone of the mantle (Fig. 13), which suggests a maximum pressure not exceeding 2 GPa (O'Neill, 1981). To better constrain the wehrlite formation pressure conditions, their modal compositions were examined. There is evidence for the simultaneous crystallization of olivine and clinopyroxene, which show 'finger-like' microtexture in the NGVF wehrlite xenoliths (Fig. 2d). This texture suggests reaction of the basaltic liquid and peridotite (Kelemen, 1990) to produce not only clinopyroxene, but olivine as well. Such microtextures have also been observed in experimental runs (Shaw, 1999) and natural occurrences (e.g., Zinngrebe and Foley, 1995). The 72–82 vol.% (av.: 76 vol.%) olivine modes in NGVF wehrlite xenoliths are better constrained and somewhat higher than those of previously published lherzolite xenoliths representing all lherzolite groups in the central NGVF (65–81 vol.%, av.: 71 vol.% in Szabó and Taylor, 1994; 52–89 vol.%, av.: 75 vol.% in Liptai et al., 2017). The narrow range for olivine modes in wehrlites suggests that the metasomatism led to a uniform olivine volume, independent of the precursor modal composition. The NGVF wehrlites probably do not have higher olivine content because of the temperature-pressure conditions of metasomatism ($T_{Ca-in-opx}$ = 985–1055 °C; ~1–2 GPa). Shaw (1999) demonstrated that orthopyroxene dissolution creates increasing portions of clinopyroxene with decreasing amounts of olivine in experiments as pressure increases from 0.4 GPa to 2 GPa, with only minor olivine at 2 GPa. The olivine/clinopyroxene ratio, which is ~4 in the NGVF wehrlites (Table 1) and ~6, ~13, ~10 in Group IA, IB and IIB lherzolites (Liptai et al., 2017), respectively, clearly show clinopyroxene enrichment with respect to

olivine in the wehrlite xenoliths. The formation of more clinopyroxene than olivine indicates a minimum pressure of 1 GPa during wehrlitization (Shaw, 1999). This also suggests that the physical conditions of clinopyroxene formation may play a more significant role than the composition of the precursor rock or the metasomatic agent. A better estimation could be obtained using the appropriate geotherm based on the alkaline basalt province geotherm (Jones et al., 1983). The similar equilibration temperatures calculated for relicts and lherzolites suggests similar pressure ranges also. Based on these similarities, we propose that the wehrlites were derived from a depth of 40–50 km (1.3–1.6 GPa) which is in good agreement with that of lherzolite xenoliths of Liptai et al. (2017) (Fig. 13). This estimated depth is greater than the wide range of 12–37 km (0.4–0.9 GPa and 0.9–1.2 GPa) assumed for NGVF cumulates that occasionally contain plagioclase (Kovács et al., 2004; Zajacz et al., 2007, respectively) and the 25 ± 5 km for local Moho (Klébesz et al., 2015) (Fig. 13).

*9.5. Numerical modelling of rare earth element behavior during wehrlitization*

In order to test our hypothesis for wehrlite formation that involves interaction between a mafic metasomatic agent and the precursor lherzolite (Fig. 10; Table 7), REE numerical modelling was carried out using the plate model of Vernières et al. (1997). This model simulates the chromatographic effects of porous fluid flow, taking complex mantle processes into account, such as melt extraction related to molten peridotite compaction, polybaric melt segregation or fluid-matrix reactions accompanied by melt infiltration (Vernières et al., 1997). Therefore, the plate model is often applied for understanding REE behavior during metasomatism.

It is necessary to constrain the compositions of both reactants for the plate models. The most plausible mafic melt agent is represented by the NGVF alkali basalt. However, the only available chemical compositions for the non-fractionated and non-contaminated mafic melt, i. e., the silicate melt inclusions from the NGVF (Zajacz et al., 2007), lack data for several REE, which weakens the results of the modelling. Therefore, we applied the trace element dataset of Sun and McDonough (1989) for a reactant melt with OIB composition, which is in good agreement with the assumed local basalt composition and closest to the presumed metasomatic melt character (Fig. 10; Table 7). Among the four lherzolite xenolith groups of Liptai et al. (2017), Group IA and IB were selected as available lherzolite sources in the modelling, both of which are present in the central NGVF. The Group IA xenoliths have uniformly depleted REE patterns (Fig. 6a in Liptai et al., 2017), whereas the group IB xenoliths have variable REE concentrations (Fig. 6b in Liptai et al., 2017). Therefore, we created a IB/1 subgroup having convex upward ($La_N/Lu_N > 2$) and a IB/2 subgroup displaying a mostly flat REE distribution ($La_N/Lu_N < 2$). Thus, we applied the average modal and REE compositions of these three lherzolite groups (IA, IB/1, IB/2), respectively, and simulated interactions with the reactant OIB melt (Supplementary Table 7).

In the model of Vernières et al. (1997), simplified melt-rock interaction zones are created, based on both natural samples and theoretical considerations. In our modelling, we applied these well-constrained melt-rock reaction zone boundaries, which structurally consist of: (1) extensive orthopyroxene, clinopyroxene and moderate olivine dissolution; (2) orthopyroxene and clinopyroxene dissolution accompanied by olivine precipitation; (3) dissolution of orthopyroxene and precipitation of olivine; (4) dissolution of orthopyroxene and precipitation of clinopyroxene. The petrography of the wehrlite xenoliths also confirms that olivine (Fig. 2e, discussed above in section 9.2.3.) and orthopyroxene (Fig. 2g) dissolution are likely to occur. The possibility that precursor clinopyroxenes melted as well cannot be excluded because of the elevated temperatures during melt infiltration. In addition to the dissolution reactions, the precipitation of new phases is also observable in wehrlite xenoliths, such as the elongated olivines in clinopyroxene-rich patches (Fig. 2d) or clinopyroxene at the expense of orthopyroxene
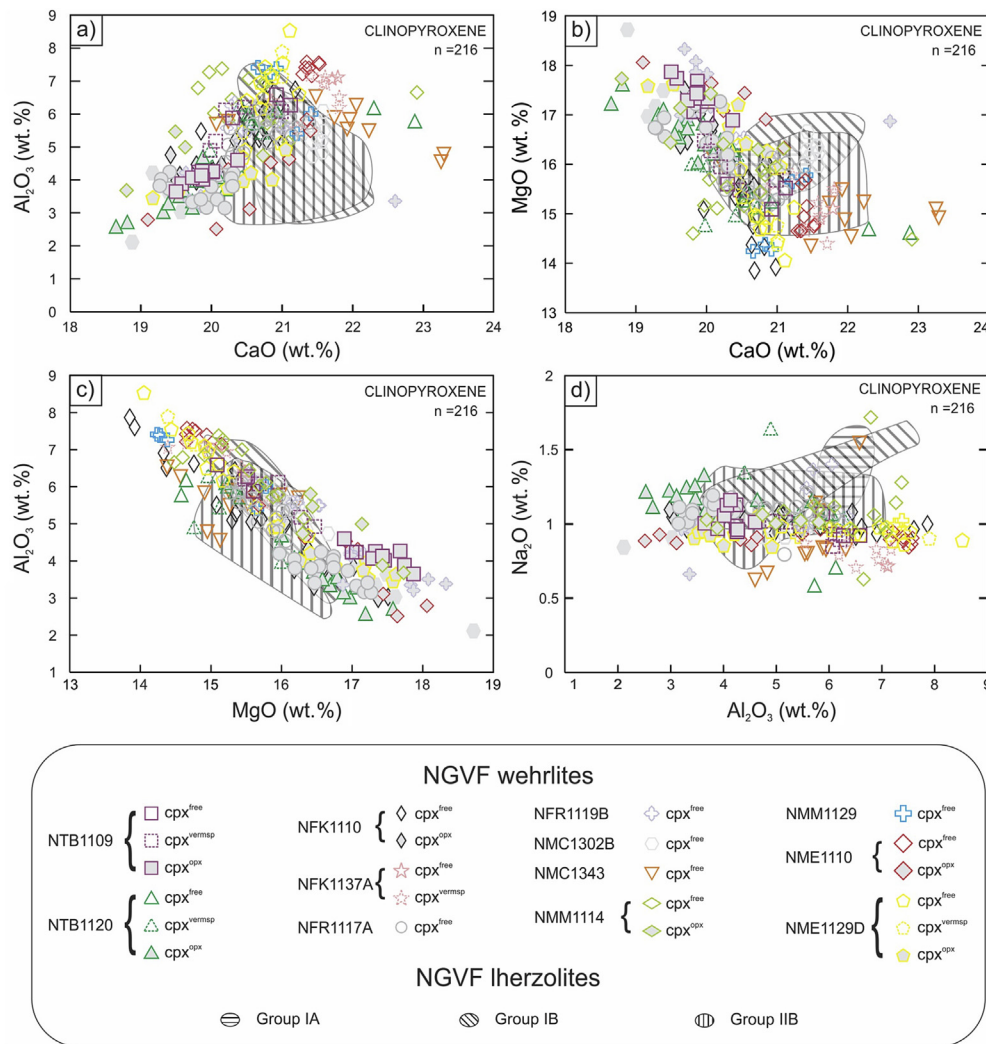
**Fig. 11.** Major element compositions of wehrlitic clinopyroxenes appearing in different textural positions compared to distinct NGVF lherzolites of Liptai et al. (2017). **(a)** CaO vs. $Al_2O_3$; **(b)** CaO vs. MgO; **(c)** MgO vs. $Al_2O_3$; **(d)** $Al_2O_3$ vs. $Na_2O$. (cpx$^{free}$–vermicular spinel and orthopyroxene free clinopyroxenes; cpx$^{vermsp}$–clinopyroxenes hosting vermicular spinel; cpx$^{opx}$–clinopyroxenes hosting orthopyroxene).

(Fig. 2g). The partition coefficients used in the modelling are from Ionov et al. (2002), because these workers report data for all REE.

The modelling results predict similar modal proportion changes (Supplementary Tables 5, 8, 9) regardless of the precursor (Supplementary Table 7). Cells located close to the reaction front are dunites, followed by wehrlites with no orthopyroxenes, wehrlites with orthopyroxenes, clinopyroxene-rich lherzolites (cpx > opx) and orthopyroxene-rich lherzolites (cpx < opx), respectively (Supplementary Tables 8, 9, 10).

In order to determine the most realistic model output, i.e., that which best describes the precursor (i.e. best fitting cell), the measured (in the thin section) and computed (modelled) REE concentrations were compared to each other by calculating the sum of the squared differences. The model (Supplementary Table 11) that shows the best fit to the data is characterized by the lowest sum of the square values calculated from the measured and modelled values. This method is similar to the calculation of the mean squared error (MSE) applied generally in regression analysis (Montgomery et al., 2012).

Comparison of the bulk REE patterns between the best fitting cells and the NGVF wehrlites resulted in mostly good agreement (Fig. 14). In four xenoliths (NTB1120, NFR1117A, NMC1302B, NMM1129) the best fitting cells were obtained using a depleted Group IA lherzolite precursor

(Fig. 14). In the rest of the xenoliths (NTB1109, NFK1110, NFK1137A, NMC1343, NMM1114, NME1110, NME1129D) the assumed precursor is Group IB/2 lherzolite with a flat REE pattern and in one case (NFR1119B) the precursor is Group IB/1 lherzolite with convex upward REE pattern. This suggests that all Group IA and IB lherzolites are potential precursors, demonstrating that the wehrlitization occurred after the formation of mantle domains with these geochemical characteristics. Another important observation is that wehrlitization results in the affected mantle domain having uniform petrographic and geochemical characteristics (as indicated by the similar bulk REE patterns of the NGVF wehrlites), regardless of variations in the precursor lherzolites (Supplementary Fig. 4).

In addition to the bulk REE patterns, the modal compositions of the chosen modelled cells (Supplementary Tables 8, 9, 10) were compared to the NGVF wehrlites (Table 1). Accordingly, the best fitting cells are dominantly wehrlites (Table 8), but with lower clinopyroxene contents and a narrower modal range (11–14 vol.%) compared to the NGVF wehrlites (10–24 vol.%; Table 1). The only exception is xenolith NFR1119B, where the best fitting cell is a clinopyroxene-rich lherzolite (Table 8). The modelled melt/rock ratios are mostly between 0.30 and 0.33 (Table 8), with the exception of xenoliths NTB1109, NFR1119B and xenoliths NFR1117A, NMC1302B and NMM1129, in which the lowest
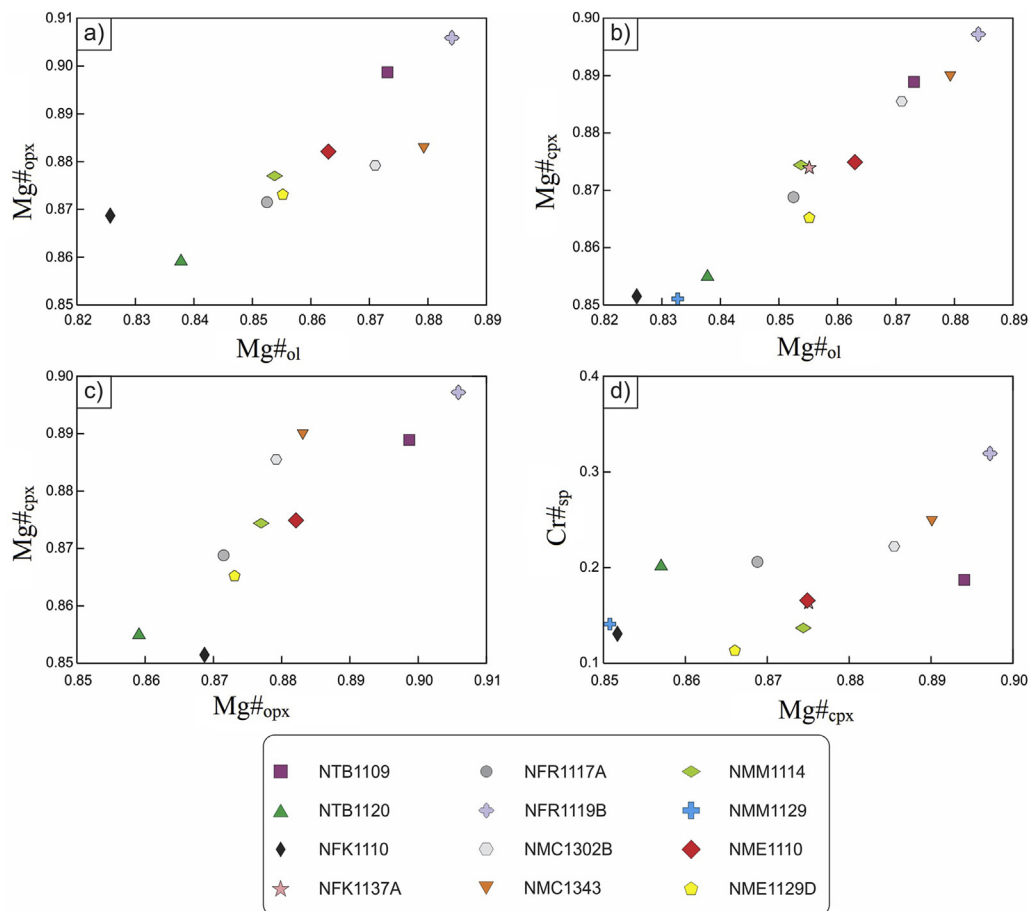
**Fig. 12.** Relationships between **(a)** $Mg\#_{ol}$ vs. $Mg\#_{opx}$, **(b)** $Mg\#_{ol}$ vs. $Mg\#_{cpx}$, **(c)** $Mg\#_{opx}$ vs. $Mg\#_{cpx}$, **(d)** $Mg\#_{cpx}$ vs. $Cr\#_{sp}$. Note that the Cr# of the vermicular spinels was excluded in evaluating the averages.

(0.22 and 0.18) and the highest (0.39, 0.39 and 0.37) melt/rock ratios were observed, respectively. These values are in good agreement with experimental results simulating the wehrlitization process (discussed above in section 9.2.3.). Xenoliths NTB1109 and NFR119B are weakly metasomatized, whereas NFR1117A and NMM1129 are significantly

affected by the metasomatic agent (Fig. 12), indicating that the degree of the metasomatism and the melt/rock ratio correlates. The high modelled melt/rock ratio (0.39) in xenolith NMC1302B is accompanied by high Mg# (0.87 in olivine and 0.89 in clinopyroxene) and flat, type II clino-pyroxenes (Fig. 7b), and the reason for this behavior is unclear. However, the model fit for this xenolith was poor (Fig. 14).

In conclusion, we can reproduce the bulk REE patterns of wehrlites with the plate model using depleted IA, flat and IB precursor lherzolites with convex upward REE patterns and reactant melt with OIB composi-tion (Fig. 14). Our modelling supports the assumption of Liptai et al. (2017) that wehrlitization represents the last event in the geochemical evolution of the upper mantle beneath the NGVF. The results of the modelling also suggest that melt/rock ratio plays a key role in the degree of petrographic and geochemical transformation of the wall rock. In contrast, the characteristics of the precursors have little effect on the features of the metasomatic product, namely wehrlite.

### 9.6. Possible links between wehrlitization and Neogene volcanic events

In the Nógrád-Gömör area two distinct stages of Neogene volcanic activity whose melts could be traced to the upper mantle can be recog-nized on the surface (Fig. 1b). The older, Miocene (~16 Ma; Pécskay et al., 2006) garnet-bearing calc-alkaline andesite is represented by Karancs Hill (Lantai, 1991; Harangi et al., 2001), situated west of the Medves Plateau (Fig. 1b). It is also known that the Nógrád-Gömör upper mantle xenoliths contain hydrous minerals such as amphibole and phlogopite, whose formation is probably linked to fluids related to a prior subduction event based on their geochemistry (Szabó and Taylor, 1994; Szabó et al., 1996; Liptai et al., 2017). However, the geophysical data
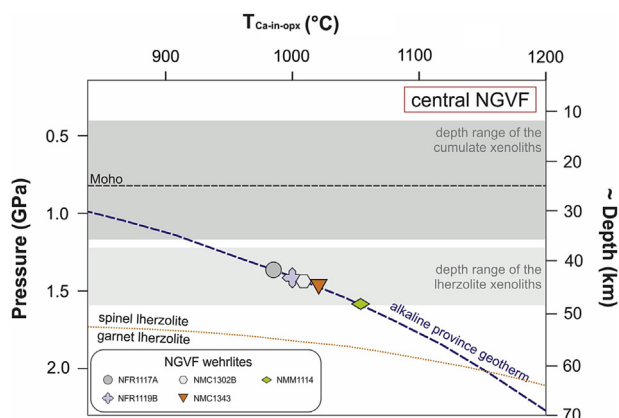


**Fig. 13.** Estimation of depth of origin for the studied xenoliths with available equilibration temperature data (Table 1) using the alkaline-province geotherm of Jones et al. (1983). The equilibration temperatures were obtained with the corrected Ca-in-opx thermometer of Nimis and Grütter (2010). The local Moho depth was estimated by Klébesz et al. (2015). The depth range for the local lherzolites was defined by Liptai (2018). The spinel lherzolite to garnet lher-zolite transformation curve ($Fo_{90}$ composition) is taken from O'Reilly et al. (1997), based on the work of O'Neill (1981).
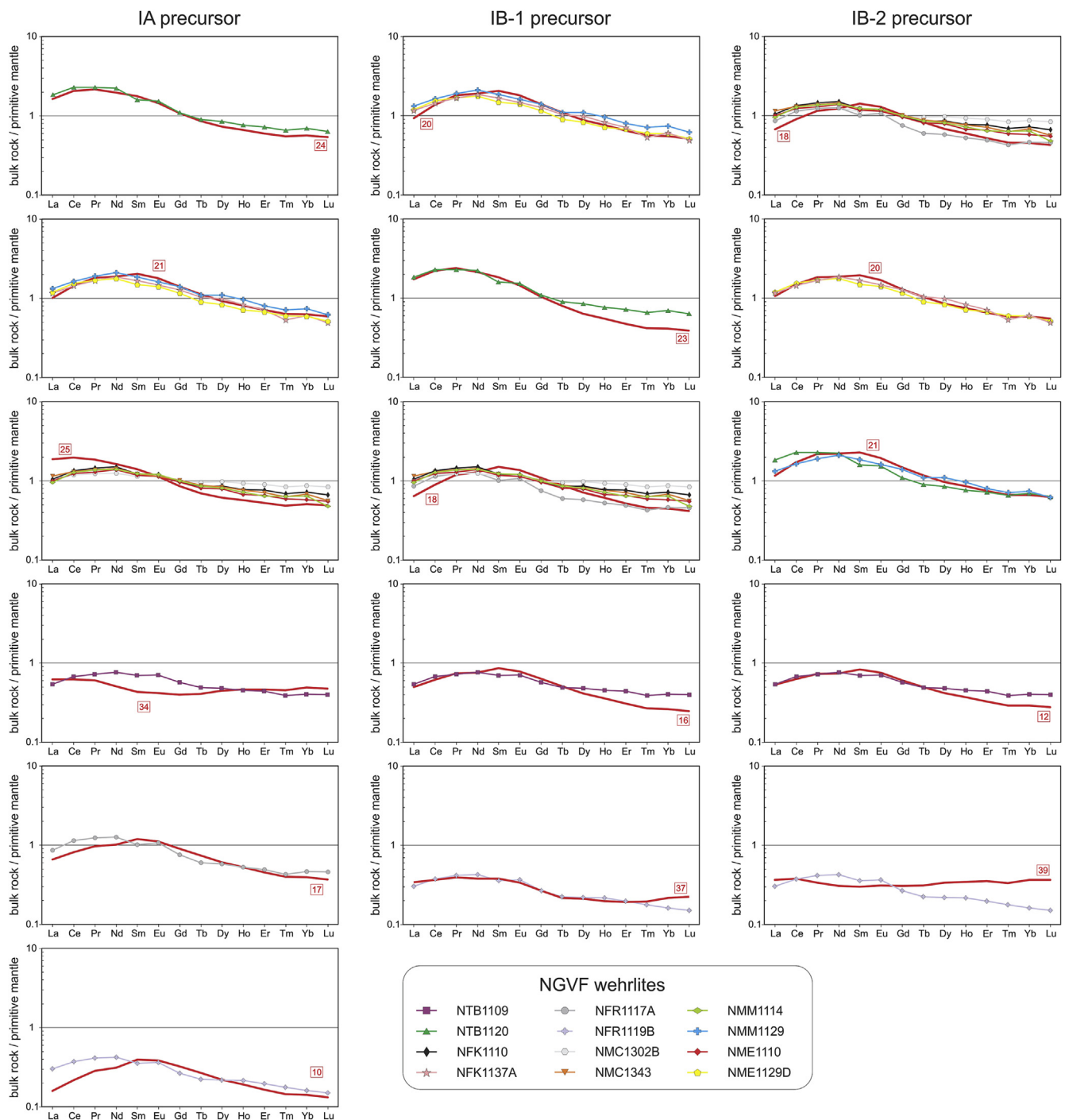
**Fig. 14.** The comparison between the bulk rock REE distributions of the NGVF wehrlites and the best fitting cells of the plate model (Vernières et al., 1997). The best fitting was determined by applying the least squares method (see details in section 9.5). The wall rock precursors of the best fitting cells are indicated and either belong to Group IA or Group IB/2 lherzolites with depleted or flat bulk rock REE patterns, respectively (based on Liptai et al., 2017).

show no evidence of subducted oceanic lithosphere remnants beneath the Western Carpathians, making the Miocene subduction highly uncertain (Grad et al., 2006; Tašárová et al., 2009 and references therein). Hence, Liptai et al. (2017) favored an inherited origin for these subduction related phases in the lherzolite xenoliths, in agreement with the interpretation of Kovács and Szabó (2008). Hence, it is unlikely that subduction-related melt had any chemical and/or physical influence on the wehrlitization process.

In contrast, melts associated with the 7–0.3 Ma (Balogh et al., 1981; Hurai et al., 2013) alkali basalts of the NGVF are interpreted to have been

derived from the asthenosphere (e.g. Embey-Isztin et al., 1993). Their trace element composition is similar to that calculated for the metasomatic melt, and these melts may have been associated with the wehrlitization process (Fig. 10; Table 7). Furthermore, the presence of orthopyroxene remnants in clinopyroxenes (Fig. 2g), intragranular compositional inhomogeneities in the rock-forming minerals (Fig. 4), and partially glassy silicate melt inclusions in clinopyroxenes and olivines (Patkó et al., 2018) all imply that the metasomatism was either ongoing or occurred shortly before the entrainment of xenoliths into host basalt. Therefore, we suggest that the melt agent associated with

**Table 8**

The best fitting modelled cell results of the plate model (Vernières et al., 1997) calculations linked to the studied wehrlites. The best fitting cells were chosen using the least squares method (see further information in section 9.5.).

| Sample | Precursor | Cell | La | Ce | Pr | Nd | Sm | Eu | Gd | Tb | Dy | Ho | Er | Tm | Yb | Lu | Melt/Rock | Rock name | ol | opx | cpx | sp | amph |
|---|---|---|---|---|---|---|---|---|---|---|---|---|---|---|---|---|---|---|---|---|---|---|---|
| NTB1109 | IB-2 | 12 | 0.346 | 1.060 | 0.185 | 0.927 | 0.337 | 0.116 | 0.331 | 0.049 | 0.283 | 0.055 | 0.143 | 0.020 | 0.129 | 0.019 | 0.220 | wehrlite | 87 | 0 | 11 | 2 | 0 |
| NTB1120 | IA | 24 | 1.065 | 3.454 | 0.553 | 2.468 | 0.721 | 0.223 | 0.589 | 0.086 | 0.496 | 0.100 | 0.264 | 0.037 | 0.249 | 0.036 | 0.330 | wehrlite | 82 | 2 | 14 | 2 | 0 |
| NFK1110 | IB-2 | 18 | 0.436 | 1.509 | 0.294 | 1.539 | 0.577 | 0.199 | 0.559 | 0.082 | 0.461 | 0.089 | 0.228 | 0.031 | 0.201 | 0.029 | 0.311 | wehrlite | 87 | 0 | 11 | 2 | 0 |
| NFK1137A | IB-2 | 20 | 0.692 | 2.490 | 0.469 | 2.333 | 0.792 | 0.260 | 0.707 | 0.102 | 0.575 | 0.112 | 0.289 | 0.040 | 0.258 | 0.037 | 0.307 | wehrlite | 86 | 0 | 12 | 2 | 0 |
| NFR1117A | IA | 17 | 0.426 | 1.355 | 0.247 | 1.272 | 0.487 | 0.172 | 0.493 | 0.073 | 0.409 | 0.079 | 0.199 | 0.027 | 0.174 | 0.025 | 0.391 | wehrlite | 86 | 0 | 13 | 2 | 0 |
| NFR1119B | IB-1 | 37 | 0.221 | 0.610 | 0.099 | 0.474 | 0.153 | 0.051 | 0.144 | 0.021 | 0.141 | 0.029 | 0.084 | 0.013 | 0.095 | 0.015 | 0.178 | cpx-rich lhz | 79 | 8 | 10 | 2 | 0 |
| NMC1302B | IA | 18 | 0.447 | 1.471 | 0.280 | 1.471 | 0.569 | 0.200 | 0.573 | 0.085 | 0.474 | 0.091 | 0.232 | 0.032 | 0.203 | 0.029 | 0.388 | wehrlite | 85 | 0 | 13 | 2 | 0 |
| NMC1343 | IB-2 | 18 | 0.436 | 1.509 | 0.294 | 1.539 | 0.577 | 0.199 | 0.559 | 0.082 | 0.461 | 0.089 | 0.228 | 0.031 | 0.201 | 0.029 | 0.311 | wehrlite | 87 | 0 | 11 | 2 | 0 |
| NMM1114 | IB-2 | 18 | 0.436 | 1.509 | 0.294 | 1.539 | 0.577 | 0.199 | 0.559 | 0.082 | 0.461 | 0.089 | 0.228 | 0.031 | 0.201 | 0.029 | 0.311 | wehrlite | 87 | 0 | 11 | 2 | 0 |
| NMM1129 | IA | 21 | 0.658 | 2.407 | 0.462 | 2.340 | 0.825 | 0.276 | 0.761 | 0.111 | 0.624 | 0.122 | 0.312 | 0.043 | 0.278 | 0.040 | 0.368 | wehrlite | 84 | 0 | 14 | 2 | 0 |
| NME1110 | IB-2 | 18 | 0.436 | 1.509 | 0.294 | 1.539 | 0.577 | 0.199 | 0.559 | 0.082 | 0.461 | 0.089 | 0.228 | 0.031 | 0.201 | 0.029 | 0.311 | wehrlite | 87 | 0 | 11 | 2 | 0 |
| NME1129D | IB-2 | 20 | 0.692 | 2.490 | 0.469 | 2.333 | 0.792 | 0.260 | 0.707 | 0.102 | 0.575 | 0.112 | 0.289 | 0.040 | 0.258 | 0.037 | 0.307 | wehrlite | 86 | 0 | 12 | 2 | 0 |

Abbreviations: ol–olivine, opx–orthopyroxene, cpx–clinopyroxene, sp–spinell, amph–amphibole, cpx-rich lhz–clinopyroxene-rich lherzolite.

wehrlitization is related to a melt generation and migration process that is linked to a magmatic event that led to the host basalt volcanism. The petrographic and geochemical features of Nógrád-Gömör wehrlite xenoliths suggest that the xenoliths initially underwent metasomatism, and then the mantle xenoliths were entrained by basaltic melt, with both events linked to the same magmatic process. According to this scenario, at least two chemically, rather homogeneous, batches of magma ascended beneath the central NGVF. One modified the peridotite mantle and resulted in formation of wehrlites (Fig. 15) and the other brought fragments of both the metasomatically altered and the pristine mantle to the surface. During the basaltic melt-peridotite interaction and fractionation in the upper mantle, modified silicate melts formed as well and orthopyroxene dissolution occurred (discussed above in section 9.2.3). Therefore, the presence of modified melts in the mantle environment is not necessarily linked to subduction. Determination of the extent of the metasomatized mantle domain and its relationship to other lithologies is difficult to evaluate because of the restricted size of the xenoliths. However, long period MT data beneath the NGVF show a low resistivity (<10 Ωm) body under the Moho (30–50 km) beneath the central part of the NGVF (Novák et al., 2014), the same area from which wehrlite xenoliths originated (Fig. 1b; Supplementary Fig. 6). Such low resisitivity values are most likely related to the presence of fluids/melt (Ádám et al., 2017). The overlap between the electrical conductivity anomaly and the wehrlite sampling localities is consistent with a genetic relationship. Based on this observation, the metasomatism affected a large volume of the mantle (~30 km long and ~15 km thick) (Novák et al., 2014), suggesting also that migration of the metasomatic melt in the upper mantle along grain boundaries was probably extensive. The melt penetration beneath the NGVF may be linked to the vertical foliation of the local lithospheric mantle (Liptai et al., 2019). However, its wider geological relationship is not yet fully explored.

## 10. Concluding remarks

(1) Wehrlites in the central part of the Nógrád-Gömör Volcanic Field (NGVF), situated in the northern margin of the Pannonian Basin in northern Hungary and southern Slovakia, display unique petrographic characteristics implying melt interaction, such as 'finger-like' microfabrics, clinopyroxene formation at the expense of orthopyroxene, and vermicular spinel crystallization. Based on the major element geochemistry of the rock-forming minerals, significant Fe, Mn, Ca Ti and Al enrichment is observed in minerals compared to lherzolite xenoliths in the NGVF. The majority of wehrlitic clinopyroxenes show convex upward REY pattern with HFSE and slight LREE enrichment.

(2) The metasomatic agent was a mafic silicate melt derived from the asthenosphere, which migrated along grain boundaries causing variable degrees of metasomatism beneath the Moho.

(3) The reaction textures of wehrlites and geochemical heterogeneities of the rock-forming minerals imply that the studied mantle domains did not achieve chemical equilibrium with the metasomatic melt before entrapment of the xenoliths in the uprising basaltic melt. Hence, we suggest that wehrlitization is associated with a recent melt generation and migration process, which is linked to the same magmatic event as the host basalt volcanism.

(4) Wehrlite xenoliths were only found in the central part of the NGVF. The distribution coincides with a high-resistivity anomaly based on long period magnetotelluric data beneath the volcanic field. Therefore, we conclude that the magnetotelluric anomaly could be linked to the metasomatism, which affected a large volume of the upper mantle (a few hundred km$^3$).

(5) According to our observations and model results, the pressure-temperature conditions and the melt/rock ratio during wehrlitization may play a more significant role than the composition of the precursor rock. This suggests that interaction of modally and

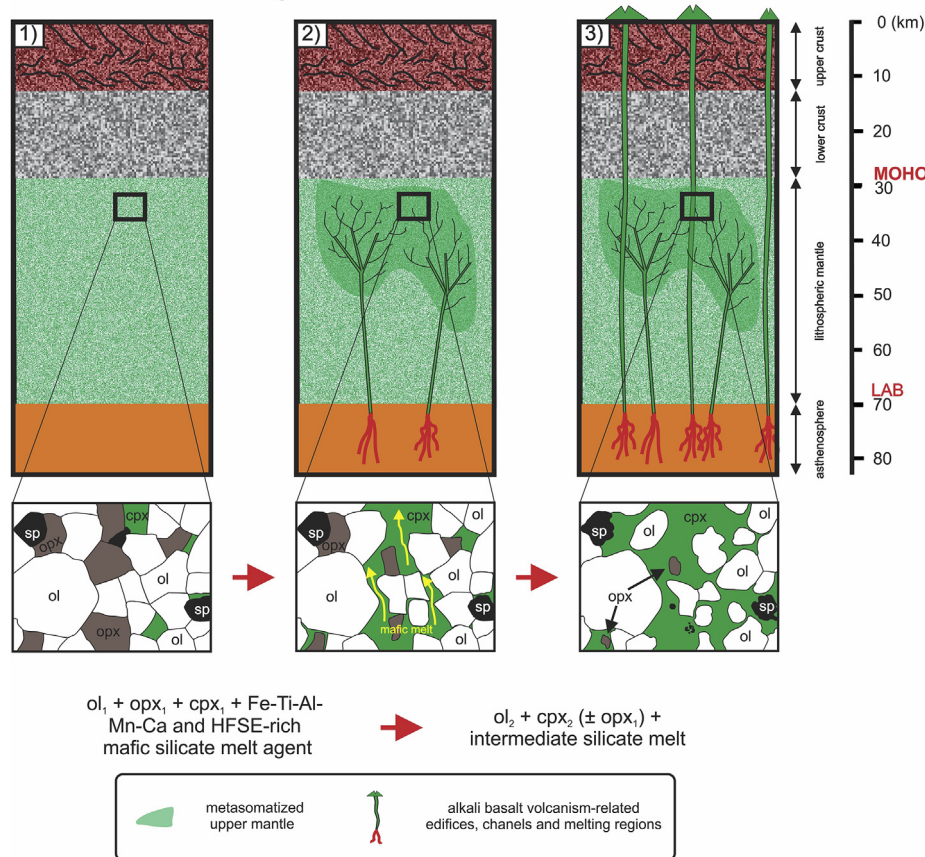## Central Nógrád-Gömör Volcanic Field



**Fig. 15.** Simplified cartoon showing the evolution model for the wehrlitization process. The local Moho and LAB (Lithosphere-Asthenosphere Boundary) depths are from Klébesz et al. (2015).

geochemically variable starting materials with a reactant melt could lead to uniform products.

## Appendix A. Supplementary data

Supplementary data to this article can be found online at https://doi.org/10.1016/j.gsf.2019.09.012.

## References

Ádám, A., Szarka, L., Novák, A., Wesztergom, V., 2017. Key results on deep electrical conductivity anomalies in the Pannonian Basin (PB), and their geodynamic aspects. Acta Geod. Geophys. 52 (2), 205–228.

Arai, S., Yurimoto, H., 1994. Podiform chromitites of the Tari-Misaka ultramafic complex, southwestern Japan, as mantle-melt interaction products. Econ. Geol. 89 (6), 1279–1288.

Bada, G., Horváth, F., 2001. On the structure and tectonic evolution of the Pannonian basin and surrounding orogens. Acta Geol. Hung. 44 (2–3), 301–327.

Balázs, A., Matenco, L., Magyar, I., Horváth, F., Cloetingh, S., 2016. The link between tectonics and sedimentation in back-arc basins: new genetic constraints from the analysis of the Pannonian Basin. Tectonics 35 (6), 1526–1559.

Bali, E., Falus, G., Szabó, C., Peate, D.W., Hidas, K., Török, K., Ntaflos, T., 2007. Remnants of boninitic melts in the upper mantle beneath the central Pannonian Basin? Mineral. Petrol. 90 (1–2), 51–72.

Balla, Z., 1984. The Carpathian loop and the Pannonian basin: a kinematic analysis. Geophys. Trans. 30 (4), 313–353.

Ballhaus, C., 1998. Origin of podiform chromite deposits by magma mingling. Earth Planet. Sci. Lett. 156 (3), 185–193.

Balogh, K., Mihaliková, A., Vass, D., 1981. Radiometric dating of basalts in southern and central Slovakia. Zapadne Karp. Ser. Geol. 7, 113–126.

Bodinier, J.L., Vasseur, G., Vernières, J., Dupuy, C., Fabries, J., 1990. Mechanisms of mantle metasomatism: geochemical evidence from the Lherz orogenic peridotite. J. Petrol. 31 (3), 597–628.

Cherniak, D.J., Liang, Y., 2007. Rare earth element diffusion in natural enstatite. Geochem. Cosmochim. Acta 71 (5), 1324–1340.

Coltorti, M., Bonadiman, C., Hinton, R.W., Siena, F., Upton, B.G.J., 1999. Carbonatite metasomatism of the oceanic upper mantle: evidence from clinopyroxenes and glasses in ultramafic xenoliths of Grande Comore, Indian Ocean. J. Petrol. 40 (1), 133–165.

Coogan, L.A., Hain, A., Stahl, S., Chakraborty, S., 2005. Experimental determination of the diffusion coefficient for calcium in olivine between 900°C and 1500°C. Geochem. Cosmochim. Acta 69 (14), 3683–3694.

Csontos, L., 1995. Tertiary tectonic evolution of the Intra-Carpathian area. Acta Vulcanol. 7, 1–14.

Csontos, L., Nagymarosy, A., 1998. The Mid-Hungarian line: a zone of repeated tectonic inversions. Tectonophysics 297 (1), 51–71.

Csontos, L., Vörös, A., 2004. Mesozoic plate tectonic reconstruction of the Carpathian region. Palaeogeogr. Palaeoclimatol. Palaeoecol. 210 (1), 1–56.

Csontos, L., Nagymarosy, A., Horváth, F., Kovac, M., 1992. Tertiary evolution of the Intra-Carpathian area: a model. Tectonophysics 208 (1), 221–241.

Dick, H.J., Fisher, R.L., Bryan, W.B., 1984. Mineralogic variability of the uppermost mantle along mid-ocean ridges. Earth Planet. Sci. Lett. 69 (1), 88–106.

Dobosi, G., Fodor, R.V., Goldberg, S.A., 1995. Late-Cenozoic alkali basalt magmatism in Northern Hungary and Slovakia: petrology, source compositions and relationships to tectonics. Acta Vulcanol. 7, 219–229.

Downes, H., 2001. Formation and modification of the shallow sub-continental lithospheric mantle: a review of geochemical evidence from ultramafic xenolith suites and tectonically emplaced ultramafic massifs of western and central Europe. J. Petrol. 42 (1), 233–250.

Downes, H., Beard, A., Hinton, R., 2004. Natural experimental charges: an ion-microprobe study of trace element distribution coefficients in glass-rich hornblendite and clinopyroxenite xenoliths. Lithos 75 (1–2), 1–17.

Embey-Isztin, A., 1978. On the petrology of spinel lherzolite nodules in basaltic rocks from Hungary and Auvergne, France. Ann. Hist.-Nat. Musei Natl. Hung. 70, 27–44.

Embey-Isztin, A., Downes, H., James, D.E., Upton, B.G.J., Dobosi, G., Ingram, G.A., Harmon, R.S., Scharbert, H.G., 1993. The petrogenesis of Pliocene alkaline volcanic rocks from the Pannonian Basin, eastern central Europe. J. Petrol. 34 (2), 317–343.

Fodor, L., Csontos, L., Bada, G., Györfi, I., Benkovics, L., 1999. Tertiary tectonic evolution of the Pannonian Basin system and neighbouring orogens: a new synthesis of palaeostress data. Geol. Soc. Lond. Spec. Publ.. 156 (1), 295–334.

Fodor, L., Jelen, B., Márton, E., Skaberne, D., Čar, J., Vrabec, M., 1998. Miocene-Pliocene tectonic evolution of the Slovenian Periadriatic fault: Implications for Alpine-Carpathian extrusion models. Tectonics 17 (5), 690–709.

Frey, F.A., Prinz, M., 1978. Ultramafic inclusions from San Carlos, Arizona: petrologic and geochemical data bearing on their petrogenesis. Earth Planet. Sci. Lett. 38 (1), 129–176.

Gaul, O.F., Griffin, W.L., O'Reilly, S.Y., Pearson, N.J., 2000. Mapping olivine composition in the lithospheric mantle. Earth Planet. Sci. Lett. 182, 223–235.

Gervasoni, F., Klemme, S., Rohrbach, A., Grützner, T., Berndt, J., 2017. Experimental constraints on mantle metasomatism caused by silicate and carbonate melts. Lithos 282, 173–186.

Girardeau, J., Francheteau, J., 1993. Plagioclase-wehrlites and peridotites on the East Pacific Rise (Hess Deep) and the Mid-Atlantic Ridge (DSDP site 334): evidence for magma percolation in the oceanic upper mantle. Earth Planet. Sci. Lett. 115 (1), 137–149.

Grad, M., Guterch, A., Keller, G.R., Janik, T., Hegedűs, E., Vozár, J., Slaczka, A., Tiira, T., Yliniemi, J., 2006. Lithospheric structure beneath trans-Carpathian transect from Precambrian platform to Pannonian basin: CELEBRATION 2000 seismic profile CEL05. J. Geophys. Res.: Solid Earth 111 (B3).

Guzmics, T., Zajacz, Z., Kodolányi, J., Halter, W., Szabó, C., 2008. LA-ICP-MS study of apatite-and K feldspar-hosted primary carbonatite melt inclusions in clinopyroxenite xenoliths from lamprophyres, Hungary: implications for significance of carbonatite melts in the Earth's mantle. Geochem. Cosmochim. Acta 72 (7), 1864–1886.

Harangi, S., 2001. Neogene to Quaternary volcanism of the Carpathian–Pannonian region—a review. Acta Geol. Hung. 44 (2), 223–258.

Harangi, S., Downes, H., Kósa, L., Szabó, C., Thirlwall, M.F., Mason, P.R.D., Mattey, D., 2001. Almandine garnet in calc-alkaline volcanic rocks of the northern Pannonian Basin (Eastern–Central Europe): geochemistry, petrogenesis and geodynamic implications. J. Petrol. 42 (10), 1813–1843.

Harangi, S., Jankovics, M.É., Sági, T., Kiss, B., Lukács, R., Soós, I., 2015. Origin and geodynamic relationships of the Late Miocene to Quaternary alkaline basalt volcanism in the Pannonian basin, eastern–central Europe. Int. J. Earth Sci. 104 (8), 2007–2032.

Hart, S.R., Dunn, T., 1993. Experimental cpx/melt partitioning of 24 trace elements. Contrib. Mineral. Petrol. 113 (1), 1–8.

Hauri, E.H., Shimizu, N., Dieu, J.J., Hart, S.R., 1993. Evidence for hotspot-related carbonatite metasomatism in the oceanic upper mantle. Nature 365 (6443), 221.

Horváth, F., 1993. Towards a mechanical model for the formation of the Pannonian basin. Tectonophysics 226 (1), 333–357.

Horváth, F., Bada, G., Szafián, P., Tari, G., Ádám, A., Cloetingh, S., 2006a. Formation and deformation of the Pannonian Basin: constraints from observational data. Geol. Soc. Lond. Mem. 32 (1), 191–206.

Horváth, F., Cloetingh, S., 1996. Stress-induced late-stage subsidence anomalies in the Pannonian basin. Tectonophysics 266 (1–4), 287–300.

Hovorka, D., Fejdi, P., 1980. Spinel peridotite xenoliths in the west Carpathian late Cenozoic alkali basalts and their tectonic significance. Bull. Volcanol. 43 (1), 95–106.

Hurai, V., Danišík, M., Huraiová, M., Paquette, J.L., Ádám, A., 2013. Combined U/Pb and (U–Th)/He geochronometry of basalt maars in Western Carpathians: implications for age of intraplate volcanism and origin of zircon metasomatism. Contrib. Mineral. Petrol. 166 (4), 1235–1251.

Ionov, D.A., Bodinier, J.L., Mukasa, S.B., Zanetti, A., 2002. Mechanisms and sources of mantle metasomatism: major and trace element compositions of peridotite xenoliths from Spitsbergen in the context of numerical modelling. J. Petrol. 43 (12), 2219–2259.

Ionov, D.A., Chanefo, I., Bodinier, J.L., 2005. Origin of Fe-rich lherzolites and wehrlites from Tok, SE Siberia by reactive melt percolation in refractory mantle peridotites. Contrib. Mineral. Petrol. 150 (3), 335–353.

Jones, A.P., Smith, J.V., Dawson, J.B., Hansen, E.C., 1983. Metamorphism, partial melting, and K-metasomatism of garnet-scapolite-kyanite granulite xenoliths from Lashaine, Tanzania. J. Geol. 91 (2), 143–165.

Kázmér, M., Kovács, S., 1985. Permian-Palaeogene palaeogeography along the eastern part of the Insubric-Periadriatic Linament system: evidence for continental escape of the Bakony-Drauzug Unit. Acta Geol. Hung. 28, 71–84.

Kelemen, P.B., 1990. Reaction between ultramafic rock and fractionating basaltic magma I. Phase relations, the origin of calc-alkaline magma series, and the formation of discordant dunite. J. Petrol. 31 (1), 51–98.

Kelemen, P.B., Dick, H.J., Quick, J.E., 1992. Formation of harzburgite by pervasive melt/rock reaction in the upper mantle. Nature 358 (6388), 635–641.

Kelemen, P.B., Hart, S.R., Bernstein, S., 1998. Silica enrichment in the continental upper mantle via melt/rock reaction. Earth Planet. Sci. Lett. 164 (1), 387–406.

Klébesz, R., Gráczer, Z., Szanyi, G., Liptai, N., Kovács, I., Patkó, L., Pintér, Z., Falus, G., Wesztergom, V., Szabó, C., 2015. Constraints on the thickness and seismic properties of the lithosphere in an extensional setting (Nógrád-Gömör Volcanic Field, Northern Pannonian Basin). Acta Geod. Geophys. 50 (2), 133–149.

Kogarko, L., Kurat, G., Ntaflos, T., 2001. Carbonate metasomatism of the oceanic mantle beneath Fernando de Noronha Island, Brazil. Contrib. Mineral. Petrol. 140 (5), 577–587.

Konečný, P., Huraiová, M., Bielik, M., 1999. P-T-X-fO$_2$ conditions in upper mantle: evidence from lherzolitic xenoliths hosted by Plio-Pleistocene alkali basalts (Southern-Slovakia). Geolines 9, 59–66.

Konečný, P., Konečný, V., Lexa, J., Huraiová, M., 1995. Mantle xenoliths in alkali basalts of Southern Slovakia. Acta Vulcanol. 7, 241–247.

Kovács, I., Szabó, C., 2008. Middle Miocene volcanism in the vicinity of the Middle Hungarian zone: evidence for an inherited enriched mantle source. J. Geodyn. 45 (1), 1–17.

Kovács, I., Falus, G., Stuart, G., Hidas, K., Szabó, C., Flower, M.F.J., Hegedűs, E., Posgay, K., Zilahi-Sebess, L., 2012. Seismic anisotropy and deformation patterns in upper mantle xenoliths from the central Carpathian–Pannonian region: asthenospheric flow as a driving force for Cenozoic extension and extrusion? Tectonophysics 514, 168–179.

Kovács, I., Zajacz, Z., Szabó, C., 2004. Type-II xenoliths and related metasomatism from the Nógrád-Gömör Volcanic Field, Carpathian-Pannonian region (northern Hungary–southern Slovakia). Tectonophysics 393 (1), 139–161.

Kovács, I.J., Kiss, J., Török, K., Király, E., Karátson, D., Fancsik, T., Biró, T., Pálos, Z., Aradi, L.E., Patkó, L., Liptai, N., Falus, G., Hidas, K., Wesztergom, V., Szabó, C., 2018. A new conceptual model for the genesis of Plio-Pleistocene alkaline basalts in the Pannonian Basin. Geophys. Res. Abstr. 20, EGU2018–9929.

Lantai, C., 1991. Genetics of garnets from andesites of the Karancs Mountains. Acta Geol. Hung. 34/ (1–2), 133–154.

Lee, W.J., Wyllie, P.J., 1997. Liquid immiscibility between nephelinite and carbonatite from 1.0 to 2.5 GPa compared with mantle melt compositions. Contrib. Mineral. Petrol. 127 (1–2), 1–16.

Lexa, J., Seghedi, I., Németh, K., Szakács, A., Konečný, V., Pécskay, Z., Fülöp, A., Kovacs, M., 2010. Neogene-Quaternary volcanic forms in the Carpathian-Pannonian Region: a review. Cent. Eur. J. Geosci. 2 (3), 207–270.

Liptai, N., Hidas, K., Tommasi, A., Patkó, L., Kovács, I., Tommasi, A., O'Reilly, S.Y., Griffin, W.L., Pearson, N.J., Szabó, C., 2019. Lateral and vertical heterogeneity in the lithospheric mantle at the margin of a continental extensional basin system reconstructed from peridotite xenolith microstructures (northern Pannonian Basin). J. Geophys. Res.: Solid Earth 124 (7), 6315–6336. https://doi.org/10.1029/2018JB016582.

Liptai, N., Patkó, L., Kovács, I.J., Hidas, K., Pintér, Z., Jeffries, T., Zajacz, Z., O'Reilly, S.Y., Griffin, W.L., Pearson, N.J., Szabó, C., 2017. Multiple metasomatism beneath the Nógrád–Gömör Volcanic Field (Northern Pannonian Basin) revealed by upper mantle peridotite xenoliths. J. Petrol. 58 (6), 1107–1144.

Liptai, N., 2018. Geochemical and Physical Properties and Evolution of the Lithospheric Mantle beneath the Nógrád-Gömör Volcanic Field (Northern Pannonian Basin, Central Europe). Ph.D. thesis. Macquarie University and Eötvös University, p. 176.

McDonough, W.F., Sun, S.S., 1995. The composition of the Earth. Chem. Geol. 120 (3), 223–253.

Mitchell, A.L., Grove, T.L., 2016. Experiments on melt–rock reaction in the shallow mantle wedge. Contrib. Mineral. Petrol. 171 (12), 107.

Montgomery, D.C., Peck, E.A., Vining, G.G., 2012. Introduction to Linear Regression Analysis, vol. 821. John Wiley & Sons, ISBN 978-0-470-54281-1.

Morimoto, N., 1988. Nomenclature of pyroxenes. Mineral. Petrol. 39 (1), 55–76.

Mutchler, S.R., Fedele, L., Bodnar, R.J., 2008. Analysis Management System (AMS) for reduction of laser ablation ICPMS data. In: Laser-ablation-ICPMS in the Earth Sciences: Current Practices and Outstanding Issues, vol. 40. Mineralogical Association of Canada Quebec, pp. 318–327.

Navon, O., Stolper, E., 1987. Geochemical consequences of melt percolation: the upper mantle as a chromatographic column. J. Geol. 95 (3), 285–307.

Neumann, E.R., Wulff-Pedersen, E., Pearson, N.J., Spencer, E.A., 2002. Mantle xenoliths from Tenerife (Canary Islands): evidence for reactions between mantle peridotites and silicic carbonatite melts inducing Ca metasomatism. J. Petrol. 43 (5), 825–857.

Nimis, P., Grütter, H., 2010. Internally consistent geothermometers for garnet peridotites and pyroxenites. Contrib. Mineral. Petrol. 159 (3), 411–427.

Novák, A., Klébesz, R., Szabó, C., Wesztergom, V., Patkó, L., Liptai, N., Ádam, A., Semenov, V.Y., Lemperger, I., Kis, A., Gribovszki, K., 2014. Combined geophysical (magnetotellurics) and geochemical results for determination of the lithosphere-asthenosphere boundary (LAB) beneath the Nógrád–Gömör volcanic field. In: 22nd EM Induction Workshop, Weimar, Germany, p. 4.

O'Neill, H.S.C., 1981. The transition between spinel lherzolite and garnet lherzolite, and its use as a geobarometer. Contrib. Mineral. Petrol. 77 (2), 185–194.

O'Reilly, S.Y., Chen, D., Griffin, W.L., Ryan, C.G., 1997. Minor elements in olivine from spinel lherzolite xenoliths: implications for thermobarometry. Mineral. Mag. 61 (2), 257–269.

O'Reilly, S.Y., Griffin, W.L., 2013. Mantle metasomatism. In: Metasomatism and the Chemical Transformation of Rock. Springer, Berlin, Heidelberg, pp. 471–533.

Patkó, L., Liptai, N., Aradi, L.E., Bodnar, R.J., Sendula, E., Kovács, I.J., Klébesz, R., Szabó, C., 2018. Deciphering mantle metasomatism using silicate melt inclusions beneath the Nógrád-Gömör volcanic field (northern Pannonian Basin). EGU general assembly, 8-13 April, Vienna (Austria). Geophys. Res. Abstr. 20, EGU2018–E2785.

Patkó, L., Liptai, N., Kovács, I.J., Aradi, L., Xia, Q.-K., Ingrin, J., Mihály, J., O'Reilly, S., Griffin, W.L., Wesztergom, V., Szabó, C., 2019. Extremely low structural hydroxyl contents in upper mantle xenoliths from the Nógrád-Gömör Volcanic Field (northern Pannonian Basin): geodynamic implications and the role of post-eruptive re-equilibration. Chem. Geol. 507, 23–41.

Pearce, N.J., Perkins, W.T., Westgate, J.A., Gorton, M.P., Jackson, S.E., Neal, C.R., Chenery, S.P., 1997. A compilation of new and published major and trace element data for NIST SRM 610 and NIST SRM 612 glass reference materials. Geostand. Newsl. 21 (1), 115–144.

Pécskay, Z., Lexa, J., Szakács, A., Seghedi, I., Balogh, K., Konečný, V., Zelenka, T., Kovacs, M., Póka, T., Fülöp, A., Márton, E., Panaiotu, C., Cvetković, V., 2006. Geochronology of Neogene magmatism in the Carpathian arc and intra-Carpathian area. Geol. Carpathica Bratisl. 57 (6), 511.

Peslier, A.H., Francis, D., Ludden, J., 2002. The lithospheric mantle beneath continental margins: melting and melt–rock reaction in Canadian Cordillera xenoliths. J. Petrol. 43 (11), 2013–2047.

Pouchou, J.L., Pichoir, F., 1991. Quantitative analysis of homogeneous or stratified microvolumes applying the model "PAP". In: Electron Probe Quantitation. Springer US, pp. 31–75.

Raffone, N., Chazot, G., Pin, C., Vannucci, R., Zanetti, A., 2009. Metasomatism in the lithospheric mantle beneath Middle Atlas (Morocco) and the origin of Fe- and Mg-rich wehrlites. J. Petrol. 50 (2), 197–249.

Ratschbacher, L., Frisch, W., Linzer, H.G., Merle, O., 1991. Lateral extrusion in the Eastern Alps, part 2: structural analysis. Tectonics 10 (2), 257–271.

Rivalenti, G., Zanetti, A., Mazzucchelli, M., Vannucci, R., Cingolani, C.A., 2004. Equivocal carbonatite markers in the mantle xenoliths of the Patagonia backarc: the Gobernador Gregores case (Santa Cruz Province, Argentina). Contrib. Mineral. Petrol. 147 (6), 647–670.

Rocco, I., Lustrino, M., Zanetti, A., Morra, V., Melluso, L., 2013. Petrology of ultramafic xenoliths in Cenozoic alkaline rocks of northern Madagascar (Nosy Be Archipelago). J. South Am. Earth Sci. 41, 122–139.

Roduit, N., 2006. MicroVision: Image analysis toolbox for measuring and quantifying components of high-definition images. Version 1.2.2. http://www.jmicrovision.com (Accessed 02 July 2006).

Royden, L.H., Horváth, F., Burchfiel, B.C., 1982. Transform faulting, extension, and subduction in the Carpathian Pannonian region. Geol. Soc. Am. Bull. 93 (8), 717–725.

Rudnick, R.L., McDonough, W.F., Chappell, B.W., 1993. Carbonatite metasomatism in the northern Tanzanian mantle: petrographic and geochemical characteristics. Earth Planet. Sci. Lett. 114 (4), 463–475.

Saper, L., Liang, Y., 2014. Formation of plagioclase-bearing peridotite and plagioclase-bearing wehrlite and gabbro suite through reactive crystallization: an experimental study. Contrib. Mineral. Petrol. 167 (3), 1–16.

Schmid, S.M., Bernoulli, D., Fügenschuh, B., Matenco, L., Schefer, S., Schuster, R., Tischler, M., Ustaszewski, K., 2008. The Alpine-Carpathian-Dinaridic orogenic system: correlation and evolution of tectonic units. Swiss J. Geosci. 101 (1), 139–183.

Scott, J.M., Hodgkinson, A., Palin, J.M., Waight, T.E., Van der Meer, Q.H.A., Cooper, A.F., 2014. Ancient melt depletion overprinted by young carbonatitic metasomatism in the New Zealand lithospheric mantle. Contrib. Mineral. Petrol. 167 (1), 1–17.

Seghedi, I., Downes, H., Vaselli, O., Szakács, A., Balogh, K., Pécskay, Z., 2004. Post-collisional Tertiary–Quaternary mafic alkalic magmatism in the Carpathian–Pannonian region: a review. Tectonophysics 393 (1), 43–62.

Shaw, C.S., 1999. Dissolution of orthopyroxene in basanitic magma between 0.4 and 2 GPa: further implications for the origin of Si-rich alkaline glass inclusions in mantle xenoliths. Contrib. Mineral. Petrol. 135 (2–3), 114–132.

Shaw, C.S., Eyzaguirre, J., Fryer, B., Gagnon, J., 2005. Regional variations in the mineralogy of metasomatic assemblages in mantle xenoliths from the West Eifel Volcanic Field, Germany. J. Petrol. 46 (5), 945–972.

Shaw, C.S., Lebert, B.S., Woodland, A.B., 2018. Thermodynamic modelling of mantle–melt interaction evidenced by veined wehrlite xenoliths from the Rockeskyllerkopf Volcanic Complex, West Eifel Volcanic field, Germany. J. Petrol. 59 (1), 59–86.

Smith, D., Riter, J.A., Mertzman, S.A., 1999. Water–rock interactions, orthopyroxene growth, and Si-enrichment in the mantle: evidence in xenoliths from the Colorado Plateau, southwestern United States. Earth Planet. Sci. Lett. 165 (1), 45–54.

Stegena, L., Geczy, B., Horváth, F., 1975. Late cenozoic evolution of the Pannonian Basin. Tectonophysics 26 (1), 71–90.

Streckeisen, A., 1976. To each plutonic rock its proper name. Earth Sci. Rev. 12 (1), 1–33.

Suhr, G., Kelemen, P., Paulick, H., 2008. Microstructures in Hole 1274A peridotites, ODP Leg 209, Mid-Atlantic Ridge: tracking the fate of melts percolating in peridotite as the lithosphere is intercepted. Geochem. Geophys. Geosyst. 9 (3).

Sun, S.S., McDonough, W.F., 1989. Chemical and isotopic systematics of oceanic basalts: implications for mantle composition and processes. Geol. Soc. Lond. Spec. Publ. 42 (1), 313–345.

Szabó, C., Bodnar, R.J., 1996. Changing magma ascent rates in the Nógrád–Gömör volcanic field, Northern Hungary/Southern Slovakia: evidence from $CO_2$-rich fluid inclusions in metasomatized upper mantle xenoliths. Petrology 4 (3), 221–230.

Szabó, C., Bodnar, R.J., 1998. Fluid-inclusion evidence for an upper-mantle origin for green clinopyroxenes in late Cenozoic basanites from the Nógrád-Gömör Volcanic Field, northern Hungary/southern Slovakia. Int. Geol. Rev. 40 (9), 765–773.

Szabó, C., Taylor, L.A., 1994. Mantle petrology and geochemistry beneath the Nógrád-Gömör volcanic field, Carpathian-Pannonian region. Int. Geol. Rev. 36 (4), 328–358.

Szabó, C., Bodnar, R.J., Sobolev, A.V., 1996. Metasomatism associated with subduction-related, volatile-rich silicate melt in the upper mantle beneath the Nograd-Gomor volcanic field, northern Hungary/southern Slovakia; evidence from silicate melt inclusions. Eur. J. Mineral. 8 (5), 881–899.

Szabó, C., Harangi, S., Csontos, L., 1992. Review of Neogene and Quaternary volcanism of the Carpathian-Pannonian region. Tectonophysics 208 (1), 243–256.

Tašárová, A., Afonso, J.C., Bielik, M., Götze, H.J., Hók, J., 2009. The lithospheric structure of the Western Carpathian–Pannonian Basin region based on the CELEBRATION 2000 seismic experiment and gravity modelling. Tectonophysics 475 (3), 454–469.

Tursack, E., Liang, Y., 2012. A comparative study of melt-rock reactions in the mantle: laboratory dissolution experiments and geological field observations. Contrib. Mineral. Petrol. 163 (5), 861–876.

Van Den Bleeken, G., Müntener, O., Ulmer, P., 2010. Reaction processes between tholeiitic melt and residual peridotite in the uppermost mantle: an experimental study at 0.8 GPa. J. Petrol. 51 (1–2), 153–183.

Vernières, J., Godard, M., Bodinier, J.L., 1997. A plate model for the simulation of trace element fractionation during partial melting and magma transport in the Earth's upper mantle. J. Geophys. Res. 102 (B11), 24771–24784.

Woo, Y., Yang, K., Kil, Y., Yun, S.H., Arai, S., 2014. Silica- and LREE-enriched spinel peridotite xenoliths from the Quaternary intraplate alkali basalt, Jeju Island, South Korea: old subarc fragments? Lithos 208, 312–323.

Xiao, Y., Zhang, H.F., Fan, W.M., Ying, J.F., Zhang, J., Zhao, X.M., Su, B.X., 2010. Evolution of lithospheric mantle beneath the Tan-Lu fault zone, eastern North China Craton: evidence from petrology and geochemistry of peridotite xenoliths. Lithos 117 (1), 229–246.

Xu, Y., Mercier, J.C., Lin, C., Shi, L., Menzies, M.A., Ross, J.V., Harte, B., 1996. K-rich glass-bearing wehrlite xenoliths from Yitong, Northeastern China: petrological and chemical evidence for mantle metasomatism. Contrib. Mineral. Petrol. 125 (4), 406–420.

Yaxley, G.M., Crawford, A.J., Green, D.H., 1991. Evidence for carbonatite metasomatism in spinel peridotite xenoliths from western Victoria, Australia. Earth Planet. Sci. Lett. 107 (2), 305–317.

Yaxley, G.M., Green, D.H., Kamenetsky, V., 1998. Carbonatite metasomatism in the southeastern Australian lithosphere. J. Petrol. 39 (11–12), 1917–1930.

Zajacz, Z., Kovács, I., Szabó, C., Halter, W., Pettke, T., 2007. Evolution of mafic alkaline melts crystallized in the uppermost lithospheric mantle: a melt inclusion study of olivine-clinopyroxenite xenoliths, northern Hungary. J. Petrol. 48 (5), 853–883.

Zhang, H.F., Nakamura, E., Kobayashi, K., Ying, J.F., Tang, Y.J., 2010. Recycled crustal melt injection into lithospheric mantle: implication from cumulative composite and pyroxenite xenoliths. Int. J. Earth Sci. 99 (6), 1167–1186.

Zinngrebe, E., Foley, S.F., 1995. Metasomatism in mantle xenoliths from Gees, West Eifel, Germany: evidence for the genesis of calc-alkaline glasses and metasomatic Ca-enrichment. Contrib. Mineral. Petrol. 122 (1–2), 79–96.